

Quantization of surface charge density on hyperboloidal and paraboloidal domains with application to plasmon decay rate on nanoprobes

M. Bagherian,¹ S. Kouchekian,¹ I. Rothstein,¹ and A. Passian^{2,3,*}

¹*Department of Mathematics and Statistics, University of South Florida, Tampa, Florida 33620, USA*

²*Oak Ridge National Laboratory, Oak Ridge, Tennessee 37831-6123, USA*

³*Department of Physics, University of Tennessee, Knoxville, Tennessee 37996, USA*



(Received 28 June 2018; revised manuscript received 22 August 2018; published 18 September 2018)

Field quantization in high curvature geometries help understanding the elastic and inelastic scattering of photons and electrons in nanostructures and probe-like metallic domains. The results find important applications in high-resolution photonic and electronic modalities of scanning probe microscopy, nano-optics, plasmonics, and quantum sensing. We present a calculation of relevant photon interactions in both hyperboloidal and paraboloidal material domains. The two morphologies are compared for their plasmon dispersion properties, field distributions, and radiative decay rates, which are shown to be consistent with the corresponding quantities for the finite prolate spheroidal domains. The results are relevant to other material domains that model a nanostructure such as a probe tip, quantum dot, or nanoantenna.

DOI: [10.1103/PhysRevB.98.125413](https://doi.org/10.1103/PhysRevB.98.125413)

I. INTRODUCTION

Materials confined to microscopic elongated “probe-like” domains, in addition to having been tremendously enabling in various forms of scanning probe microscopy (SPM), hold great potential for emerging applications in fields such as quantum sensing [1–4]. Recent interest in the properties of such tip-shaped material domains is reflected in the demonstration of laser pulse induced electron emission from a gold solid tip under grating coupled plasmon excitation [5–7]. These applications make use of the excitation and resonant properties of surface modes on bounding surfaces and interfaces of metallic, dielectric, and metallo-dielectric domains that take the form of a tip [8]. Examples of systems that use a probe tip include scanning tunneling microscope, photon scanning tunneling microscope, apertured and apertureless nearfield scanning optical microscope, nanoantennas, and processes such as tip-enhanced spectroscopy and lithography. The intriguing excitations, typically studied near the tip apex, are expected to receive contributions not only from stationary modes, such as those occurring at the surfaces of finite nanoparticles, but also from nonstationary modes propagating at the infinite interfaces. The theoretical and modeling tools for investigating the response of these systems and their dependence specifically upon the geometric characteristics have been indispensable in the development of these applications. In particular, analytical techniques that lend themselves to provide complete or partial information on the system are often regarded as necessary not only for obtaining the system response (e.g., energy distribution in the nearfield of the nanoparticles), but also for elucidating the inner working of the systems (e.g., the contributing eigenstates and

eigenvalues). Calculation of geometric and material dependencies of surface mode excitation, decay and scattering on the bounding surfaces of nanoscale domains are both instructive and necessary for better design and fabrication.

Here, we investigate the radiative decay rate of plasmons by quantizing the surface modes engendered on the surface of a metallic probe modeled as one sheet of a two-sheeted hyperboloid of revolution, shown in Fig. 1(a). This geometry offers an elegant adaptability not only for the description of the local curvature of a fabricated probe but also for the modeling of nearly planar interfaces [8]. In addition, it has the property that the hyperboloidal domain translates along its symmetry axis when changing the opening angle θ_0 , that is, smaller $\mu_0 = \cos \theta_0$, yields smaller gap z_{\min} , the apex distance to origin o in Fig. 1(a). To provide a basis for comparison, we quantize the surface charge density oscillations on the useful system of a paraboloid of revolution, which offers a similar apex morphology but a different asymptotic behavior away from the apex. Importantly, the apex and off-apex curvature of a paraboloid of revolution presents a more natural topology for comparison of its spectral and scattering properties with that of a finite body of similar curvature, e.g., a spheroidal domain. Therefore, for the sake of validation, we extend our investigations to also study the radiative decay of plasmons excited on a prolate spheroid, which owing to its finite volume presents a more tangible system.

Our presentation is organized as follows. In Sec. II, we treat the paraboloidal plasmons. Here, within the quasistatic framework, representing the material domain with a frequency-dependent dielectric function, we derive the nonretarded plasmon dispersion relations, eigenmodes, and fields. From the classical energy of paraboloidal charge density oscillations, we then derive the Hamiltonian of the system. We then proceed to quantize the plasmon field and, employing an interaction Hamiltonian derived from the first-order perturbation

*passian@ornl.gov

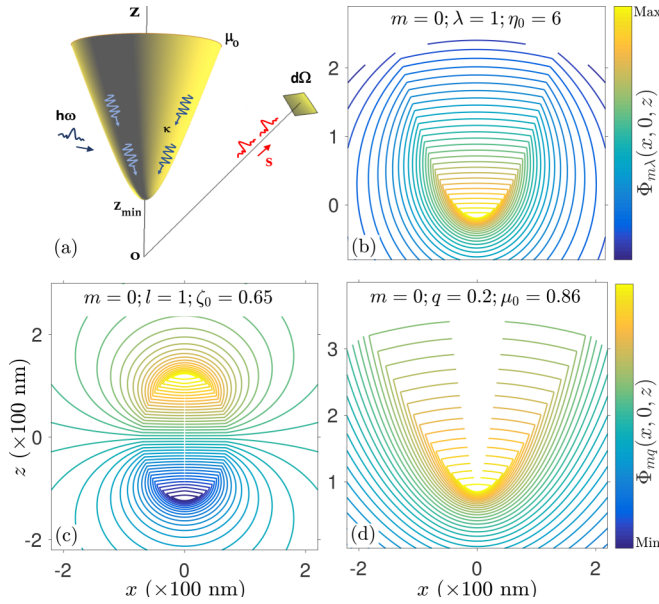


FIG. 1. Modeling systems and their potential distributions. (a) One sheet of a two-sheeted hyperboloid of revolution modeling a nanotip or a nanostructure with local curvature. Surface modes of momentum κ , e.g., excited by incoming photons $h\omega$, decay radiatively into a solid angle $d\Omega$. The curvature of the tip apex is set by the μ_0 defining the hyperboloidal surface. Here, $\mu_0 = \cos\theta_0$, where θ_0 is the angle between the z axis and an asymptote to the hyperboloidal surface such that small θ_0 yields a sharp probe while $\theta_0 \rightarrow \pi/2$ corresponds to xy plane. The apex point $z_{\min} = z_0\mu_0$, near the focal point of the hyperboloid, is set by the scale factor z_0 , as in Eq. (B1). (b), (c), and (d) show the spatial distribution of the lowest lying eigenmodes of the quasistatic electric potential for the three modeling domains investigated. For the same mode index m , optimizing the apex curvature overlap within the same spatial zx domains, and analyzing the potential distribution, leads to the determination of the corresponding continuous eigenvalues λ of the paraboloid (b) and q of the hyperboloid (d), respectively, as well as the discrete eigenvalue l of the prolate spheroid (c). The geometric parameters η_0 , μ_0 , and ζ_0 determines the form of the considered domains.

theory within the hydrodynamic model of an electron gas [9,10], obtain an analytical expression for the radiative decay rate of the plasmons. Having established the full treatment of the paraboloidal system, in Sec. III, we proceed to investigate the quantized charge density oscillations on the surface of one sheet of a two-sheeted hyperboloidal of revolution. In both these sections, the use of nonretarded potentials and dispersion relations is justified due to the subwavelength dimension of the tip. In Sec. V, we discuss our findings and compare both the paraboloidal and hyperboloidal results. An interesting comparison of the paraboloidal domain can be made with respect to the surface modes and radiation patterns of a prolate spheroid, a finite geometric domain highly suitable for modeling of nanoparticles such as a quantum dot. In specific cases, we further validate the results using computational techniques to obtain the lower energy eigenmodes and farfield radiation patterns. Concluding remarks are provided in Sec. V.

II. PLASMON EXCITATION AND RADIATIVE DECAY ON PARABOLOIDAL SURFACES

Quantum calculations that take into account the geometric effects of the bounding surfaces of the material domains are important to corroborate experimental observations in nanophysics. Here, our goal is to calculate the probability amplitude that a surface plasmon in a given initial state, engendered near the apex region of a probe-shaped material domain, will emit a photon into a given final state. To model a tiplike domain, we consider a surface of revolution about the z axis resulting in the usual azimuthal symmetry. Using two parameters r and β , such a surface can be parametrized as [11]

$$\mathbf{r} = \mathbf{r}(r, \beta) = r \cos \beta \vec{i} + r \sin \beta \vec{j} + f(r) \vec{k},$$

for any explicit equation of a surface of revolution written as $z = f(r)$, where $r = \sqrt{x^2 + y^2}$. Here, we will employ three specific cases of surfaces of revolution: a single sheet of a two-sheeted hyperboloid, a paraboloid, and a prolate spheroid. Figure 1(a) shows an example hyperboloid. In the following, we will first treat a paraboloid, for which we begin by seeking pertinent classical quantities.

A. Nonretarded potential, dispersion relations, and classical energy of surface charge density

We consider a vacuum-bounded solid paraboloid of revolution defined by $\eta = \eta_0$, via the coordinates (ξ, η, φ) given in Eqs. (A1) and (A2). Denoting the frequency ω dependent dielectric function of the paraboloidal material domain with $\varepsilon_1(\omega)$, we set the outside medium dielectric constant $\varepsilon_2 = 1$, noting that for a general case we may retain ε_2 as a parameter. The quasistatic scalar electric potential Φ is continuous everywhere in the space and satisfies the Laplace equation everywhere except on the boundary surface $\eta = \eta_0$. Employing the Laplacian in Eqs. (A3)–(A5), and considering the two resulting Sturm-Liouville problems Eqs. (A4) and (A5), with unbounded domain $\eta, \xi \in [0, \infty)$ lead to a continuous spectrum of real eigenvalues and eigenfunctions [12] in terms of Bessel and modified Bessel functions given by Eqs. (10.3.64) and (10.3.65) [13]. Using the fact that the potential is bounded on the z axis and vanishes as $r \rightarrow \infty$, together with the asymptotic behavior of the Bessel functions [14,15], we denote the potentials with Φ_i and Φ_o , for the interior and the exterior domains, respectively, and utilize the Heaviside function Θ with the half-maximum convention $\Theta(0) = 1/2$ to write the total potential as

$$\Phi(\mathbf{r}, t) = \Theta(\eta_0 - \eta)\Phi_i(\mathbf{r}, t) + \Theta(\eta - \eta_0)\Phi_o(\mathbf{r}, t),$$

or explicitly:

$$\begin{aligned} \Phi(\mathbf{r}, t) = & \sum_{m,p} S_m^p(\varphi) \int_0^\infty A_{m\lambda p}(t) J_m(\lambda \xi) \\ & \times [\Theta(\eta_0 - \eta) I_m(\lambda \eta) K_m(\lambda \eta_0) \\ & + \Theta(\eta - \eta_0) I_m(\lambda \eta_0) K_m(\lambda \eta)] d\lambda, \end{aligned} \quad (1)$$

where $m = 0, 1, 2, \dots$, and $p = 0, 1$, while $A_{m\lambda p}(t)$ are the time t dependent amplitudes to be determined by the boundary conditions, and $\{S_m^p(\varphi)\}$ indicate the azimuthal symmetry of

the eigenmodes, explicitly:

$$S_m^p(\varphi) = (2 - \delta_{0m})\delta_{0p} \cos m\varphi + \delta_{1p} \sin m\varphi,$$

satisfying the orthogonality relation given in Eq. (A16). Thus p determines the parity of the solutions. We also note that Eq. (1) guarantees the continuity of the potential across the boundary $\eta = \eta_0$. With $\vec{\nabla}^2 \Phi = 0$ for $\eta < \eta_0$ and $\eta > \eta_0$, see Eqs. (A6)–(A9), noting that the derivative of Heaviside function is the Dirac delta function $\delta(x)$, the Poisson equation for the surface charge density σ at the boundary surface $\eta = \eta_0$ implies

$$\vec{\nabla}^2 \Phi = \frac{\delta(\eta - \eta_0)}{a^2(\xi^2 + \eta^2)} \left(\frac{\partial \Phi_o}{\partial \eta} - \frac{\partial \Phi_i}{\partial \eta} \right) = -\frac{4\pi}{h_\eta} \sigma \delta(\eta - \eta_0), \quad (2)$$

where h_η , given by Eq. (A2), is a scale factor of the paraboloidal system. Therefore, solving for the charge density [following Eqs. (A10)–(A12)], we obtain

$$\sigma = \frac{1}{4\pi a \eta_0 \sqrt{\xi^2 + \eta_0^2}} \sum_{m,p} S_m^p(\varphi) \int_0^\infty A_{m\lambda p}(t) J_m(\lambda \xi) d\lambda. \quad (3)$$

If we now let n_0 denote the number density of free electrons (mass m_e and charge $-e$) in the paraboloidal domain, and \vec{u} denote the charge displacement vector, then from the definition of the polarization, the surface charge σ can be written as $\sigma = -en_0 \vec{u} \cdot \hat{\mathbf{e}}_\eta|_{\eta_0}$. Furthermore, the equation of motion for the electrons is given by $m_e \ddot{\vec{u}} = e \vec{\nabla} \Phi_i$. Thus we have $4\pi \ddot{\sigma} = -\omega_p^2 (\hat{\mathbf{e}}_\eta \cdot \vec{\nabla} \Phi_i)|_{\eta=\eta_0}$, and it follows that

$$\ddot{\sigma} = -\frac{\omega_p^2}{4\pi a \sqrt{\xi^2 + \eta_0^2}} \sum_{m,p} S_m^p(\varphi) \int_0^\infty \lambda A_{m\lambda p}(t) J_m(\lambda \xi) \times I'_m(\lambda \eta_0) K_m(\lambda \eta_0) d\lambda. \quad (4)$$

Differentiating the charge density in Eq. (3) twice with respect to time t and equating it with Eq. (4), it follows from the orthogonality of system $\{S_m^p\}_{m,p}$ that for each fixed m and p :

$$\int_0^\infty J_m(\lambda \xi) [\ddot{A}_{m\lambda p}(t) + \omega_{m\lambda}^2 A_{m\lambda p}(t)] d\lambda = 0, \quad (5)$$

where

$$\omega_{m\lambda}^2 = \omega_p^2 \lambda \eta_0 I'_m(\lambda \eta_0) K_m(\lambda \eta_0). \quad (6)$$

The (allowed) resonant values of the dielectric function ε of the paraboloid can also be independently calculated from a transcendental equation obtained by imposing the quasistatic boundary conditions at the bounding surfaces of the domain within which the scalar electric field satisfies the Laplace equation. Therefore it can be shown that $\omega_{m\lambda}$ satisfies the Drude model $1 - \varepsilon_{m\lambda} = \omega_p^2 \omega_{m\lambda}^{-2}$. Utilizing the orthogonality relation for Bessel functions given by Eq. (11.59) [16] [also see Appendix A, Eq. (A19)], it follows from Eq. (5) that the amplitudes $A_{m\lambda p}(t)$ undergo harmonic oscillations at continuous frequencies $\omega_{m\lambda}$ given by Eq. (6), that is

$$\ddot{A}_{m\lambda p}(t) + \omega_{m\lambda}^2 A_{m\lambda p}(t) = 0. \quad (7)$$

The harmonic behavior of the field amplitudes will play an essential role in the possibility of analytically calculating the

energy of the paraboloidal charge system prior to quantization.

Having obtained closed form expressions for the potential and induced surface charge density, we are now in the position to calculate the potential energy V due to the polarization charge distribution ρ as $V = \frac{1}{2} \int_\Omega \rho \Phi d\Omega$, where Ω denotes the entire space. Since ρ is only confined to the paraboloidal surface $\eta = \eta_0$ and vanishes elsewhere in the space, one may integrate over an infinitesimal thin cover across the boundary: $\eta_0 - \epsilon \leq \eta \leq \eta_0 + \epsilon$. Letting $\epsilon \rightarrow 0^+$ and making the observation $\rho h_\eta = \delta(\eta - \eta_0) \sigma$, the potential energy can be expressed as a surface integral given in Eq. (A15). From the orthogonality relations for the trigonometric system $\{S_m^p(\varphi)\}$ and the Bessel functions along with the property of the delta function, see Eqs. (A13)–(A19) in Appendix A, we obtain the potential

$$V = \frac{a}{8} \sum_{m,p} \hat{\delta}_{mp} \int_0^\infty \frac{I_m(\lambda \eta_0) K_m(\lambda \eta_0)}{\lambda} [A_{m\lambda p}(t)]^2 d\lambda, \quad (8)$$

where $\hat{\delta}_{mp}$ is given in Eq. (A17).

We will now seek the kinetic energy T of the paraboloidal charge system. Employing the charge displacement vector, we write $T = \frac{1}{2} m_e n_0 \int_\Omega \vec{u} \cdot \ddot{\vec{u}} d\Omega$. To obtain an expansion for \vec{u} , we note that in the expression for the potential Φ_i given by Eq. (1), one may use the harmonic oscillator equation Eq. (7) for the amplitudes to replace $A_{m\lambda p}(t)$ with $-\ddot{A}_{m\lambda p}(t)/\omega_{m\lambda}^2$. As a result, integrating the charge displacement vector with respect to time, we obtain: $m_e \ddot{\vec{u}} = -e \nabla \Psi$, where

$$\Psi(\mathbf{r}, \mathbf{t}) = \sum_{m,p} S_m^p(\varphi) \int_0^\infty \frac{A_{m\lambda p}(t)}{\omega_{m\lambda}^2} J_m(\lambda \xi) \times I_m(\lambda \eta) K_m(\lambda \eta_0) d\lambda. \quad (9)$$

With this expression in the integral for kinetic energy, followed by utilization of the Gauss theorem and orthogonality relations for $\{S_m^p\}$ and Bessel functions, see Eqs. (A20)–(A24) in Appendix A, we can calculate the kinetic energy as

$$T = \frac{a}{8} \sum_{m,p} \hat{\delta}_{mp} \int_0^\infty \frac{I_m(\lambda \eta_0) K_m(\lambda \eta_0)}{\lambda \omega_{m\lambda}^2} [\dot{A}_{m\lambda p}(t)]^2 d\lambda. \quad (10)$$

In view of Eqs. (8) and (10), we find that the total classical energy E of the paraboloidal system takes the following form:

$$E = \frac{a}{8} \sum_{m,p} \hat{\delta}_{mp} \int_0^\infty \frac{I_m(\lambda \eta_0) K_m(\lambda \eta_0)}{\lambda \omega_{m\lambda}^2} \times \{[\dot{A}_{m\lambda p}(t)]^2 + \omega_{m\lambda}^2 [A_{m\lambda p}(t)]^2\} d\lambda,$$

which is the total energy of the surface plasmon field, suitable for quantization.

B. Field quantization and interaction of plasmons with photons

To obtain the quantized plasmon field, the expression for the classical field E needs to be rewritten in a suitable form. We begin by noting that since the potential together with the paraboloidal harmonics $I_m(\lambda \eta)$, $J_m(\lambda \xi)$, $K_m(\lambda \eta)$, and $S_m^p(\varphi)$ are all real-valued, we have that the amplitudes $A_{m\lambda p}(t)$ are real-valued and satisfy the harmonic oscillator equation Eq. (7). Therefore toward converting E into the

Hamiltonian operator for a scalar boson field (plasmons are spinless quasiparticles), we write

$$A_{m\lambda p}(t) = \frac{\alpha_{mp\lambda}}{2\omega_{m\lambda}} [a_{m\lambda p}(t) + a_{m\lambda p}^*(t)], \quad (11)$$

where $a_{m\lambda p}$ are complex-valued time dependent functions proportional to $e^{-i\omega_{m\lambda}t}$, and $\alpha_{mp\lambda}$ are some real-valued constants to be determined later. The time derivative of Eq. (11) can now be expressed as

$$\dot{A}_{m\lambda p}(t) = \frac{i\alpha_{mp\lambda}}{2} [a_{m\lambda p}^*(t) - a_{m\lambda p}(t)]. \quad (12)$$

Performing field quantization [17,18], we replace the amplitudes $a_{m\lambda p}(t)$ and $a_{m\lambda p}^*(t)$ with operator valued distributions $\hat{a}_{m\lambda p}$ and its conjugate $\hat{a}_{m\lambda p}^\dagger$, and note the commutation relations $[\hat{a}_{m\lambda p}, \hat{a}_{m'\lambda'p'}^\dagger] = \delta_{mm'}\delta_{pp'}\delta(\lambda - \lambda')$. The continuous spectrum of the eigenvalues λ originates from the infinite axial dimension of the paraboloid. Taking the normal ordered expansion of the noncommuting boson creation $\hat{a}_{m\lambda p}^\dagger$ and annihilation $\hat{a}_{m\lambda p}$ operators, a comparison with the normal ordered expression of the Hamiltonian operator for a scalar boson field [17], yields the Hamiltonian

$$\mathcal{H}_{sp} = \sum_{m,p} \int_0^\infty \hbar\omega_{m\lambda} \hat{a}_{m\lambda p}^\dagger \hat{a}_{m\lambda p} d\lambda, \quad (13)$$

if we choose

$$\alpha_{m\lambda p}^2 = \frac{8\hbar\lambda\omega_{m\lambda}^3\delta_{mp}^{-1}}{aI_m(\lambda\eta_0)K_m(\lambda\eta_0)}. \quad (14)$$

For the interaction of the plasmon system with a photon field with Hamiltonian \mathcal{H}_p , we require the plasmon-photon interaction Hamiltonian \mathcal{H}_i , which is required to determine the radiative decay rate of surface plasmons excited on the paraboloidal surface. Our full system, plasmon field + photon field is described by the tensor product of the Fock spaces for the two constituent fields. Here, to describe the plasmon-photon interaction, we resort to the hydrodynamical formulation of the electron gas by Crowell and Ritchie [10] and utilize the Hamiltonian: $\mathcal{H}_i = \frac{1}{c} \int \mathbf{J} \cdot \mathbf{A} d\Omega$, where \mathbf{J} is the induced current density and \mathbf{A} is the vector potential operator of the photon field, see Eqs. (A25) in Appendix A. This interaction has been used previously to describe the emission of photons via plasmon decay on finite surfaces of an oblate spheroid modeling silver nanoparticles vacuum evaporated on a dielectric substrate [19]. Here, we will apply this Hamiltonian to modeling the creation of a plasmon on the surface of the paraboloid by a photon or the decay of a paraboloidal plasmon and emission of a photon [17]. This application requires the explicit determination of the current density operator, which in light of the displacement operator $\hat{u} = -(e/m_e)\vec{\nabla}\hat{\Psi}$, can be written as $\mathbf{J} = -(n_0e^2/m_e)\vec{\nabla}\hat{\Psi}$.

To write the photon field as a sum with discrete momentum eigenstates as opposed to the continuous representation, we consider our electromagnetic field to be confined to a volume \mathcal{V} , which is normally taken to be represented by a cube. Taking the electromagnetic energy confined to a volume to be independent of the shape of the volume [20,21], we take as our quantization volume a paraboloidal structure given by

$\xi = \eta = L$ with $L \gg \eta_0$. The volume is then found to be $\frac{\pi}{2}L^6$. In the paraboloidal coordinates, ξ and η have dimensions of length^{1/2} and so our volume has dimension L^3 . The transition to the discrete sum then follows the lattice strategy in quantum electrodynamics [22]:

$$\frac{1}{(2\pi)^{3/2}} \int d^3s \rightarrow \frac{1}{\sqrt{\mathcal{V}}} \sum_{\mathbf{s}}, \quad (15)$$

and $\delta(s - s') = \delta_{ss'}$. Hence we write the discretized vector potential as

$$\mathbf{A} = \sum_{\mathbf{s}} \sum_{j=1,2} \sqrt{\frac{\hbar c^2}{\mathcal{V}\omega_{\mathbf{s}}}} \hat{\mathbf{e}}_j(\hat{c}_{\mathbf{s}j} e^{i\mathbf{s}\cdot\mathbf{r}} + \hat{c}_{\mathbf{s}j}^\dagger e^{-i\mathbf{s}\cdot\mathbf{r}}), \quad (16)$$

with \mathbf{s} being the three-dimensional photon wave vector $\omega_{\mathbf{s}} = sc$, and $\hat{c}_{\mathbf{s}j}^\dagger$ and $\hat{c}_{\mathbf{s}j}$, the photon creation and annihilation time-dependent operators, while $\hat{\mathbf{e}}_j$, the polarization vector being perpendicular to \mathbf{s} for both values of j , satisfy the commutation relations $[\hat{c}_{\mathbf{s}j}, \hat{c}_{\mathbf{s}'j}^\dagger] = \delta_{jj'}\delta(\mathbf{s} - \mathbf{s}')$. For the physical quantities of interest in our work, we find that the quantization volume \mathcal{V} cancels out in our calculations. The photon field Hamiltonian corresponding to the vector potential above is $\mathcal{H}_p = \sum_{\mathbf{s}j} \hbar\omega_{\mathbf{s}} \hat{c}_{\mathbf{s}j}^\dagger \hat{c}_{\mathbf{s}j}$.

Taking \mathbf{A} to be in the radiation gauge with both $\Phi = 0$ and $\vec{\nabla} \cdot \mathbf{A} = 0$, we note $(\vec{\nabla}\hat{\Psi}) \cdot \mathbf{A} = \vec{\nabla} \cdot (\hat{\Psi}\mathbf{A})$, since the current is confined to the surface of the paraboloid, we have

$$\mathcal{H}_i = \frac{n_0e^2}{cm_e} \int_0^{2\pi} \int_0^\infty (\hat{\Psi}\mathbf{A} \cdot \hat{\mathbf{e}}_\eta) h_\xi h_\varphi d\xi d\varphi. \quad (17)$$

Differentiating $\hat{\Psi}$ given by Eq. (9) with respect to time and replacing $\dot{A}_{m\lambda p}(t)$ using Eq. (12), we can now write the interaction Hamiltonian as

$$\begin{aligned} \mathcal{H}_i &= \frac{n_0e^2}{2im_e} \sum_{\mathbf{s}} \sum_{j=1,2} \sqrt{\frac{\hbar}{\mathcal{V}\omega_{\mathbf{s}}}} (\hat{\mathbf{e}}_\eta \cdot \hat{\mathbf{e}}_j) (\hat{c}_{\mathbf{s}j} e^{i\mathbf{s}\cdot\mathbf{r}} + \hat{c}_{\mathbf{s}j}^\dagger e^{-i\mathbf{s}\cdot\mathbf{r}}) \\ &\times \sum_{m,p} \int_0^{2\pi} \int_0^L \left[\int_0^\infty S_p^m(\varphi) J_m(\lambda\xi) I_m(\lambda\eta_0) K_m(\lambda\eta_0) \right. \\ &\times \left. \frac{\alpha_{m\lambda p}(t)}{\omega_{m\lambda}^2} (\hat{a}_{m\lambda p}^\dagger - \hat{a}_{m\lambda p}) d\lambda \right] h_\xi h_\varphi d\xi d\varphi, \quad (18) \end{aligned}$$

where we have taken the integral in ξ to be from 0 to L now since our integral over space is bounded by $\xi = L$.

Having obtained the explicit form of the interaction Hamiltonian, we now aim to calculate the probability amplitude that a surface plasmon in a given initial state, defined by m , λ , and p will emit a j -polarized photon in \mathbf{s} state with momentum $\hbar\mathbf{s}$. The total radiative decay rate for a given initial state, $\gamma_{m\lambda p}$, is obtained by summing over final photon states, $\gamma_{m\lambda p} = \sum_{\mathbf{s}} \sum_{j=1,2} \gamma_{m\lambda p}^{(js)}$, where by the Fermi Golden rule, the transition probabilities are

$$\gamma_{m\lambda p}^{(js)} = \frac{2\pi}{\hbar} |\mathcal{M}_{m\lambda p}^{(js)}|^2 \delta(\omega_{\mathbf{s}} - \omega_{m\lambda}) \quad (19)$$

with $\mathcal{M}_{m\lambda p}^{(js)} = |\langle 0 | \hat{c}_{j\mathbf{s}f} \mathcal{H}_i \hat{a}_{m\lambda p}^\dagger | 0 \rangle|$ denoting the emission matrix elements, f the final state, and i the initial state,

invoking the commutation properties

$$\langle 0 | \hat{a}_{m\lambda p} \hat{a}_{m'\lambda' p'}^\dagger | 0 \rangle = \delta_{mm'} \delta(\lambda - \lambda') \delta_{pp'}, \quad (20)$$

$$\langle 0 | \hat{c}_{s'q'} \hat{c}_{sq}^\dagger | 0 \rangle = \delta(\mathbf{s} - \mathbf{s}') \delta_{qq'}, \quad (21)$$

the nonvanishing terms yield

$$\mathcal{M}_{m\lambda p}^{(js)} = \frac{n_0 e^2}{2i m_e} \sqrt{\frac{\hbar}{\mathcal{V} \omega_s}} \frac{\alpha_{m\lambda p}}{\omega_{m\lambda}^2} I_m(\lambda \eta_0) K_m(\lambda \eta_0) \mathcal{I}_{m\lambda}^{(j)}, \quad (22)$$

where we have dropped the i and f for convenience and

$$\mathcal{I}_{m\lambda}^{(j)} = \int_0^{2\pi} \int_0^L S_m^p(\varphi) (\hat{\mathbf{e}}_\eta \cdot \hat{\mathbf{e}}_j) J_m(\lambda \xi) e^{-is \cdot \mathbf{r}} h_\xi h_\varphi d\xi d\varphi. \quad (23)$$

For an arbitrary photon wave vector of the form

$$\mathbf{s} = \frac{\omega_s}{c} (\cos \psi, 0, \sin \psi),$$

we may consider the polarization vectors $\hat{\mathbf{e}}_j$ for s and p polarizations, being perpendicular and parallel to $\hat{\mathbf{z}}s$ plane, respectively, noting $\mathbf{s} \cdot \hat{\mathbf{e}}_j = 0$. Thus we consider the polarization vectors $\hat{\mathbf{e}}_1 = (0, 1, 0)$ and $\hat{\mathbf{e}}_2 = (\sin \psi, 0, -\cos \psi)$. Under these polarization conditions, Eq. (23) leads to two different integrals to be calculated:

$$\mathcal{I}_{m\lambda}^{(1)} = a \eta_0 \int_0^{2\pi} \int_0^L \xi^2 \sin \varphi E_{m\lambda}(\eta, \xi) J_m(\lambda \xi) S_m^p(\varphi) d\xi d\varphi \quad (24)$$

and

$$\begin{aligned} \mathcal{I}_{m\lambda}^{(2)} &= a \eta_0 \int_0^{2\pi} \int_0^L (\xi^2 \sin \psi \cos \varphi + \xi \eta \cos \psi) \\ &\times E_{m\lambda}(\eta, \xi) J_m(\lambda \xi) S_m^p(\varphi) d\xi d\varphi, \end{aligned} \quad (25)$$

where $E_{m\lambda}(\eta, \xi) = e^{-iA}$ with A given by

$$A = -\frac{a\omega_s}{c} \left[\xi \eta_0 \cos \psi \cos \varphi + \frac{\sin \psi (\xi^2 - \eta_0^2)}{2} \right].$$

Thus, depending on the choice of the polarization vector $\hat{\mathbf{e}}_j$, each integral contributes to a polarization state. In other words, $\mathcal{I}_{m\lambda}^{(1)}$ represents the s polarization and $\mathcal{I}_{m\lambda}^{(2)}$ corresponds to the p polarization. For a photon emitted pointing to the solid angle $d\Omega$ as depicted in Fig. 1(a), final photon states results in a continuous energy spectrum. Hence we let the quantization volume \mathcal{V} go to infinity so that we have a continuum s states, that is,

$$\sum_s \rightarrow \frac{\mathcal{V}}{(2\pi)^3} \int s^2 ds \int d\Omega, \quad (26)$$

where $\mathcal{V}/(2\pi)^3$ is the density of photon states per polarization. In view of transition probability given in Eq. (19), the radiative decay rate per unit solid angle may be written as

$$\frac{d\gamma_{m\lambda p}}{d\Omega} = \sum_{j=1,2} \frac{\mathcal{V}}{(2\pi)^3} \int \gamma_{m\lambda p}^{(js)} s^2 ds,$$

in which using $\omega_s = sc$, we obtain the final expression

$$\frac{d\gamma_{m\lambda p}}{d\Omega} = \sum_{j=1,2} \frac{\mathcal{V}}{(2\pi)^3} \frac{\omega_{m\lambda}^2}{c^3} \left[\frac{2\pi}{\hbar^2} |\mathcal{M}_{m\lambda p}^{(js)}|^2 \right]_{\omega_s = \omega_{m\lambda}}, \quad (27)$$

which is observed to be independent of the volume \mathcal{V} as it cancels out with \mathcal{V}^{-1} in $|\mathcal{M}_{m\lambda p}^{(js)}|^2$. Thus we can take our quantization volume to be infinite and convert the sum over the photon states to an integral. Hence the paraboloidal decay rate per solid angle is given by

$$\begin{aligned} \frac{d\gamma_{m\lambda p}}{d\Omega} &= \frac{\lambda \delta_{mp}^{-1}}{4\pi c^3} \left(\frac{n_0 e^2}{m_e} \right)^2 I_m(\lambda \eta_0) K_m(\lambda \eta_0) \\ &\times [(\mathcal{I}_{m\lambda}^{(1)})^2 + (\mathcal{I}_{m\lambda}^{(2)})^2], \end{aligned} \quad (28)$$

where $\mathcal{I}_{m\lambda}^{(1)}$ and $\mathcal{I}_{m\lambda}^{(2)}$ are given by Eqs. (24) and (25), respectively, and must be computed numerically.

III. PLASMON EXCITATION AND RADIATIVE DECAY ON HYPERBOLOIDAL SURFACES

Similar to the paraboloidal case, the hyperboloidal domain, shown in Fig. 1(a), is highly relevant for modeling of electronic and photonic response of probe-like nanostructures [8]. Under the same assumptions as the paraboloidal case [see Eqs. (B1)–(B8) in Appendix B], the potential now takes the form

$$\begin{aligned} \Phi(\mathbf{r}, t) &= \sum_{m=0}^{\infty} H_m(\varphi) \int_0^{\infty} A_{mq}(t) P_{mq}(\eta) \\ &\times [\Theta(\mu - \mu_0) P_{mq}(-\mu_0) P_{mq}(\mu) \\ &+ \Theta(\mu_0 - \mu) P_{mq}(\mu_0) P_{mq}(-\mu)] dq, \end{aligned} \quad (29)$$

where $A_{mq}(t)$ are real time dependent amplitudes and $H_m(\varphi) = (2 - \delta_{0m}) \cos m\varphi$, and, for convenience, we use $P_{mq}(\cdot)$ to denote $P_{-\frac{1}{2}+iq}^m(\cdot)$.

Following Eqs. (A6)–(A9) in Appendix A, the surface charge density σ on $\mu = \mu_0$ is found to be

$$\begin{aligned} \sigma &= \frac{-1}{4\pi z_0} \sqrt{\frac{1 - \mu^2}{\eta^2 - \mu_0^2}} \sum_m H_m(\varphi) \\ &\times \int_0^{\infty} A_{mq}(t) P_{mq}(\eta) \mathcal{W}_{mq}(\mu_0) dq, \end{aligned}$$

where the Wronskian identity for $\mathcal{W}_{mq}(\mu_0)$ is given in Eq. (B13). It follows from the orthogonality relation for the system $\{H_m(\varphi)\}$, given in Eq. (B9), that for each fixed $m = 0, 1, 2, \dots$, we have

$$\begin{aligned} \int_0^{\infty} P_{mq}(\eta) [\mathcal{W}_{mq}(\mu_0) \ddot{A}_{mq}(t) \\ + \omega_p^2 P_{mq}(-\mu_0) P'_{mq}(\mu_0) A_{mq}(t)] dq = 0. \end{aligned} \quad (30)$$

Applying the Van Nostrand orthogonality relation for the conical functions given in Eq. (B6) and the exact expression for the Wronskian given in Eq. (B14), it follows from Eq. (30) that for each fixed m and $q \geq 1$ the amplitudes $A_{mq}(t)$ satisfy the harmonic oscillator model $\ddot{A}_{mq}(t) + \omega_{mq}^2 A_{mq}(t) = 0$, where the frequencies ω_{mq}^2 are given by

$$\omega_{mq}^2 = \frac{\omega_p^2 \pi \sqrt{1 - \mu_0^2}}{2Z_q^m \cosh(\pi q)} P_{mq}(-\mu_0) P'_{mq}(\mu_0), \quad (31)$$

with Z_q^m defined by (B15). Again, these resonant values can also be independently calculated from the transcendental equation generated by satisfying the boundary conditions.

To calculate the classical energy E , we follow the exact same argument as in the case of a paraboloid outlined in Sec. II and Appendix A. Consequently, using the orthogonality relations in the hyperboloidal case given by Eqs. (B9) and (B6), one finds the hyperboloidal energy:

$$E = \frac{z_0}{4\pi} \sqrt{1 - \mu_0^2} \sum_m \delta_{0m} \int_0^\infty \frac{[Z_q^m \cosh(\pi q)]^2}{q \sinh(\pi q) \omega_{mq}^2} \times P_{mq}(-\mu_0) P_{mq}(\mu_0) \{[\dot{A}_{mq}(t)]^2 + \omega_{mq}^2 [A_{mq}(t)]^2\} dq. \quad (32)$$

Using similar ansatz for $A_{mq}(t)$ and $\dot{A}_{mq}(t)$ as in Eqs. (11) and (12), the coefficients α_{mq}^2 can be obtained by a comparison of Eq. (32) with the Hamiltonian Eq. (13) as

$$\alpha_{mq}^2 = \frac{4\pi \hbar \delta_{0m}^{-1}}{z_0 \sqrt{1 - \mu_0^2}} \frac{q \omega_{mq}^3 \sinh(\pi q)}{[Z_q^m \cosh(\pi q)]^2 P_{mq}(-\mu_0) P_{mq}(\mu_0)}, \quad (33)$$

where δ_{0m} is given by Eq. (B10).

Utilizing Eq. (16) and the hyperboloidal analog of Eq. (17), setting up the plasmon current density, the interaction Hamiltonian for the photon emission can be expressed as

$$\mathcal{H}_i = \frac{n_0 e^2}{2i m_e} \sum_s \sum_{j=1,2} \sqrt{\frac{\hbar}{\mathcal{V} \omega_s}} (\hat{\mathbf{e}}_\mu \cdot \hat{\mathbf{e}}_j) [\hat{c}_{sj} e^{is \cdot \mathbf{r}} + \hat{c}_{sj}^\dagger e^{-is \cdot \mathbf{r}}] \times \sum_m \int_0^{2\pi} \int_1^L \left[\int_0^\infty H_m(\varphi) P_{mq}(\eta) P_{mq}(-\mu_0) P_{mq}(\mu) \times \frac{\alpha_{mq}}{\omega_{mq}^2} (\hat{a}_{mq}^\dagger - \hat{a}_{mq}) dq \right] h_\varphi h_\eta d\varphi d\eta. \quad (34)$$

Thus we may calculate the hyperboloidal emission matrix element as

$$\mathcal{M}_{mq}^{(js)} = \frac{n_0 e^2}{2i m_e} \sqrt{\frac{\hbar}{\mathcal{V} \omega_s}} \frac{\alpha_{mq}}{\omega_{mq}^2} P_{mq}(-\mu_0) P_{mq}(\mu_0) \mathcal{I}_{mq}^{(j)}, \quad (35)$$

where for different polarization directions, we obtain

$$\mathcal{I}_{mq}^{(1)} = -z_0 \mu_0 \sqrt{1 - \mu_0^2} \int_0^{2\pi} \int_1^L \sqrt{\eta^2 - 1} P_{mq}(\eta) \times \sin \varphi H_m(\varphi) E_{mq}(\eta, \varphi) d\eta d\varphi \quad (36)$$

and

$$\mathcal{I}_{mq}^{(2)} = z_0 \sqrt{1 - \mu_0^2} \int_0^{2\pi} \int_1^L P_{mq}(\eta) \times [\mu_0 \sqrt{\eta^2 - 1} \sin \psi \cos \varphi + \sqrt{1 - \mu_0^2} \cos \psi \eta] \times H_m(\varphi) E_{mq}(\eta, \varphi) d\eta d\varphi, \quad (37)$$

where we have put $E_{mq}(\eta, \varphi) = e^{-i\mathcal{B}}$ with

$$\mathcal{B} = \frac{z_0 \omega_s}{c} \left[\sqrt{(\eta^2 - 1)(1 - \mu_0^2)} \cos \psi \cos \varphi + \mu_0 \sin \psi \eta \right].$$

The wave vector \mathbf{s} and the polarization vectors $\hat{\mathbf{e}}_1, \hat{\mathbf{e}}_2$ remain the same as before. Moreover, similar to the case for paraboloid, the choice of the polarization vector $\hat{\mathbf{e}}_j$ in each integral determines the polarization state. Hence $\mathcal{I}_{mq}^{(1)}$ represents the s polarization and $\mathcal{I}_{mq}^{(2)}$ corresponds to the p polarization. Using Eq. (33) in Eq. (27), and now the position vector in hyperboloidal coordinates given by Eq. (B1), we arrive at

$$\frac{d\gamma_{mq}}{d\Omega} = \frac{q \sinh(\pi q) \delta_{0m}^{-1} \left(\frac{n_0 e^2}{m_e} \right)^2 P_{mq}(-\mu_0) P_{mq}(\mu_0)}{4\pi z_0 c^3 \sqrt{1 - \mu_0^2} [Z_q^m \cosh(\pi q)]^2} \times [(\mathcal{I}_{mq}^{(1)})^2 + (\mathcal{I}_{mq}^{(2)})^2]. \quad (38)$$

IV. PLASMON EXCITATION AND RADIATIVE DECAY ON PROLATE SPEROIDAL SURFACES

In order to provide a geometric basis for comparison, we now treat the case of plasmon excitation on the surface of a prolate spheroidal domain. This structure presents an almost identical curvature to that of the paraboloid but encompasses a finite domain, making the interpretation of the surface modes and their associated radiation patterns more tangible. The closely related structure of an oblate spheroid has been employed in previous plasmon studies [19]. In both prolate and oblate systems, a limiting case is that of a sphere [10,17], which can serve to validate the results. To obtain the quantized surface modes of the prolate spheroid, we closely follow the oblate case [19].

A prolate spheroid is defined by fixing the coordinate $\eta = \eta_0$ in coordinate system given in Eq. (B1). The quasistatic scalar potential for a spheroid defined by $\zeta = \zeta_0$ may then be written as

$$\Phi(\mathbf{r}, t) = \sum_{m,l,p} A_{mlp}(t) Y_{lm}^p(\mu, \varphi) [\Theta(\zeta_0 - \zeta) P_l^m(\zeta) \times Q_l^m(\zeta_0) + \Theta(\zeta - \zeta_0) P_l^m(\zeta_0) Q_l^m(\zeta)], \quad (39)$$

for some real coefficients $A_{mlp}(t)$, with $l = 1, 2, 3, \dots, m = 0, \dots, l, p = 0, 1$ and $P_l^m(\cdot)$ and $Q_l^m(\cdot)$ being the associated Legendre polynomial of first and second kind, respectively, while $Y_{lm}^p(\mu, \varphi)$ are the real spherical harmonics [Eq. (C1)]. The allowed values of the dielectric function ε_{lm} are then found to be

$$\varepsilon_{lm} = 1 - \frac{(l+m)!}{(\zeta_0^2 - 1)(l-m)!} \left[\frac{(-1)^m}{P_l^m(\zeta_0) Q_l^m(\zeta_0)} \right], \quad (40)$$

following similar steps for Eqs. (1)–(6). We then obtain the matrix elements for photon emission,

$$\mathcal{M}_{lm}^{(js)} = \frac{z_0 \omega_p^2 (-i)^l \alpha_{lmp}}{2\omega_{lm}^2} \sqrt{\frac{\hbar}{\mathcal{V} \omega_s}} P_l^m(\zeta_0) Q_l^m(\zeta_0) \times \hat{\mathbf{e}}_j \cdot \vec{\nabla}_{s'} [j_l(z_0 \bar{s}) Y_{lm}^p(\bar{\theta}, \bar{\varphi})], \quad (41)$$

using an initial expression as in Eq. (C3), similar to the oblate spheroidal case in [19], with $\hat{\mathbf{e}}_j$ being the unit polarization vector for the emitted light, $j_l(\cdot)$ a spherical Bessel function of order l [see Eq. (C5)], and $\vec{\nabla}_{s'}$ the gradient of the wave vector given in spherical coordinates (s', θ', φ') , where α_{lmp} ,

and using the classical energy as

$$\alpha_{lmp}^2 = \frac{8\pi\hbar}{z_0} \frac{(-1)^{m+1} (l-m)! \omega_{lm}^3}{(l+m)! P_l^m(\zeta_0) Q_l^m(\zeta_0)}.$$

Following the same quantization scheme as before, the radiative decay rate of plasmons per unit solid angle Ω , is then calculated to be

$$\frac{d\gamma_{lmp}}{d\Omega} = \sum_{j=1,2} \frac{z_0 \omega_{lm}^4 (1 - \varepsilon_{lm}(\omega_{lm})) P_l^m(\zeta_0)}{c^3 (\zeta^2 - 1) P_l^m(\zeta_0)} \times [F_{lmp}^{(j)}(s, \theta, \varphi)]^2, \quad (42)$$

where

$$F_{lmp}^{(j)}(s, \theta, \varphi) = \frac{j_l(z_0 s'')}{s} \left[\delta_{1j} \sqrt{\zeta_0^2 - 1} \frac{\partial Y_{lm}^p(\theta'', \varphi'')}{\partial \theta''} + \delta_{2j} \frac{\zeta_0}{\sin \theta} \frac{\partial Y_{lm}^p(\theta'', \varphi'')}{\partial \varphi''} \right],$$

with $(s'', \theta'', \varphi'')$ denoting the wave vector in spherical coordinate for which the transformations are given in Eq. (C6) and for the two polarization states s and p [19].

V. RESULTS AND DISCUSSIONS

The harmonic functions, making up the eigenmodes of the hyperboloidal and paraboloidal systems, represent the normal modes of the charge density. The infinite axial dimension of these domains results in the corresponding eigenvalues (λ and q) to form continuous spectra as opposed to the discrete value spectrum (l) of finite domains such as spheroidal particles. While this difference in the nature of the eigenvalues is less noticeable when visualizing the potentials, as seen in Figs. 1(b)–1(d), it becomes noteworthy when performing the quantization since now an integration over the corresponding eigenvalue spectrum enters the Hamiltonian, Eqs. (18) and (34). However, an inspection of the asymptotic properties of the integrands in the Hamiltonians reveal fast convergence facilitating the calculation of the needed matrix elements. To proceed, we note that for a more reasonable comparison of the two systems, their physical dimensions must be made comparable. Therefore we geometrically adjust the paraboloid and the hyperboloid so as to control and match their apex curvature and further match it with that of a finite prolate spheroidal domain. The latter, due to its finite domain, makes a natural case to validate the findings for the two infinite domain cases investigated.

For settings consistent with nanofabrication and photon scattering experiments involving gold probes, where strong plasmon excitation has been reported [7,23], we employ the following settings: $\eta_0 = 60$ nm and $\mu_0 = 86$ nm for the systems in Figs. 1(b)–1(d). The close relationship of the calculated eigenvalues with the surface plasmon momenta are clearly observable from the “wavelength” of the charge density oscillations in Figs. 1(b)–1(d) and 7. For proper geometric and modal adjustments, the similarities in the potential distributions are clearly evident from the contour plots. Since for the argument values $\mu \approx 1, -1$, the conical functions become singular, a numerical artifact in the form of a discontinuity in the contour lines appear near the symmetry axis of the hyperboloids, where μ attains those values. Comparison with

the corresponding potential distribution in the spheroidal case can be facilitated by taking $\zeta_0 = 65$ nm matching its curvature with that of the apexes in paraboloidal and hyperboloidal domains. With the dimensions adjusted, using Eqs. (1), (29), and (39) to simulate the spatial distributions of the potentials for the three cases, one clearly observes the analogous role of λ and q to the discrete spectrum l . The lowest azimuthal mode $m = 0$ for the three domains shown in Figs. 1(b)–1(d) was simulated by taking the second indices as $\lambda = 1, q = 0.2$, and $l = 1$, generating relatively same potential distributions. The potential distributions for higher modes are shown in Fig. 6, where two higher modes for each domain (shape parameters η_0, μ_0 and ζ_0) are shown. In doing so, the Legendre functions $P_{mq}(\mu)$ of imaginary order and their derivatives have been calculated using the computational algorithm of Gil and Segura [24], and the integral expansion of Kölbig [25]. Analogous to plasmon wave vector in the case of excitations on a planar interface (or a Cartesian thin film), which can be emulated by $\mu_0 \rightarrow \pi/2$ in Fig. 1(a), the higher the λ, q , and l for the same m , the higher the number of fluctuations for the same spatial domains, as shown in Fig. 7. Furthermore, from the spheroidal nearfield distribution, one can readily observe the multipole order so that $(m, l) = (0, 1)$ corresponds to a dipolar distributions, whereas $(m, l) = (0, 2)$ leads to a quadrupolar behavior, etc. Similarly, for $(m, q) = (0, 1.5)$ or $(m, \lambda) = (0, 2)$, one obtains the corresponding multipolar nearfield distributions of the apex regions. Thus, guided by these charge density oscillations, controlled by the parameters (m, λ, η_0) , (m, q, μ_0) , and (m, l, ζ_0) for the three cases and by a geometric matching of their apex curvatures, one may discuss the eigenmode dependent radiative decay rates.

In addition to the material-specific electronic and optical properties, in as far as the effect of the local curvature is concerned, we expect the considered cases to exhibit similarities in their resonance spectra. The plasmon dispersion relations are good indicators of this resemblance. To study the relation between resonance modes of isolated solid paraboloids and hyperboloids in vacuum, we assume a local dielectric function and calculate their eigenmode dependent allowed values $\varepsilon_{m\lambda}$ and ε_{mq} using Eqs. (6) and (31). A comparison of the lowest lying plasmon modes ($m = 0, 1, 2$, and 3 of fixed probes η_0 and μ_0) is given in Fig. 2. The modes may alternatively be displayed with reference to bulk plasma frequency ω_p . Interestingly, the higher m modes show a higher sensitivity to the morphological differences between the two systems, in particular for lower λ and q values, that is, in the long wavelength limit, which in analogy with the planar plasmons would be near the light line, where retardation effects are more pronounced [8]. We also note that in the hyperboloidal case, in the limit $\mu_t \rightarrow 0$, we have $\varepsilon_{mq} \rightarrow -1$; that is, the modes asymptotically approach the surface plasmon resonance ($\omega \rightarrow \omega_p/\sqrt{2}$), as expected for a Cartesian half-space. This limit is also approached by large m values as seen in Fig. 2. In the short-wavelength regime $\lambda, q \rightarrow \infty$, the dielectric function reads

$$\varepsilon_{mq} \sim -1 - \frac{\cot(\theta_r)}{q}, \quad (43)$$

yielding the same surface plasmon limit [8,26]. Similar to the paraboloidal case, using the asymptotic behavior of modified Bessel functions $I_m(\lambda\eta)$ and $K_m(\lambda\eta)$ for large order m and

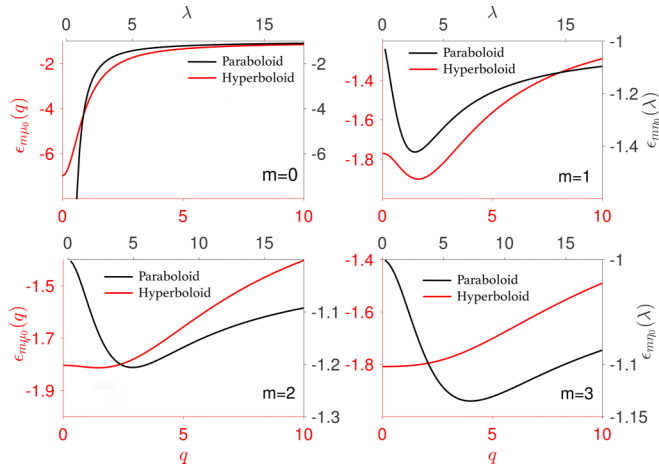


FIG. 2. Paraboloidal and hyperboloidal nonretarded surface plasmon dispersion relations. The resonance values of the dielectric function ϵ are shown for low lying modes as a function of the continuous eigenvalue λ for a paraboloid (black) and q for a hyperboloid (red). The surfaces of the paraboloid and hyperboloid are set by the parameter η_0 and μ_0 , respectively. The discrete modes are denoted by m for the azimuthal oscillations.

large arguments λ and η (see Eqs. (9.7.8) and (9.7.9) in Ref. [27]), we can write

$$\epsilon_{m\lambda} \sim -1 - \frac{1}{2\lambda\eta}, \quad (44)$$

which implies the same limit for large λ .

Following the field distribution and resonant dielectric values corresponding to the normal modes of the surface charge density oscillations, we may assume that a plasmon has been created in a given eigenmode (m, o, p) where $o = \lambda, q, l$ designating the paraboloid, the hyperboloid and the spheroid, respectively. If the plasmons on the paraboloidal, hyperboloidal or spheroidal surface are in the initial state $\hat{a}_{(mop)_i}^\dagger |0\rangle$, the probability amplitude for their emission into the final photon state $\hat{c}_{(sj)_f}^\dagger |0\rangle$ could be obtained using expressions (22), (35) and (41). The $|0\rangle$ indicates that the fields have been populated with 0 plasmons or photons (noting $a_{mop} |0\rangle = c_{(sj)} |0\rangle = 0$) whereas a general photon-plasmon state is written as $|\Psi\rangle = |n_{sj}\rangle \otimes |n_{mop}\rangle$, that is, a state with n_{sj} j -polarized photons of momentum \mathbf{s} , and n_{mop} plasmons in the (m, o, p) state.

Keeping the mode patterns, here, the $\varphi = 0, \pi$ -plane projection of the relative potential distributions in Figs. 1(b)–1(d) and dispersion relations in Fig. 2 in mind, we now compare the radiative decay rate per solid angle of plasmons engendered on the three domains, using Eq. (28) (paraboloid with $\eta_0 = 60$ nm), Eq. (38) (hyperboloid with $\mu_0 = 86$ nm) and Eq. (42) (prolate spheroid with $\zeta_0 = 65$ nm) for two lowest azimuthal mods $m = 0$ and 1. To calculate the matrix elements given in Eqs. (22) and (35), the integrations $\mathcal{I}_{m\lambda}^{(j)}$ and $\mathcal{I}_{mq}^{(j)}$ (in case for paraboloid and hyperboloid, respectively) must be carried out numerically as they lack analytical solutions in variable ξ in the case for paraboloid and η in the case for hyperboloid. The choice of polarization vectors $\hat{\mathbf{e}}_j$ for $j = 1, 2$ corresponds to $\mathcal{I}_{m\lambda}^{(1)}$ given by Eq. (24) to represent the s polarization, and

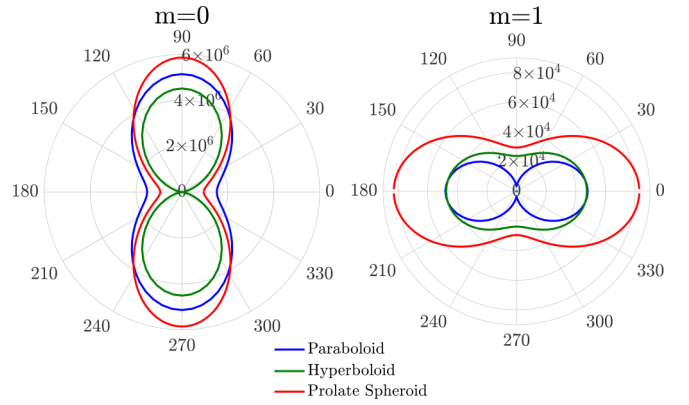


FIG. 3. The radiative decay rate of plasmons engendered on paraboloidal, hyperboloidal, and prolate spheroidal surfaces. The decay rate of paraboloidal plasmons (blue) is computed from Eq. (28) for the single eigenmode $m = 0$ (right), $m = 1$ (left) and $\lambda = 1$ when the shape parameter is $\eta_0 = 60$ nm. Similarly, the decay rate of hyperboloidal plasmons (green) computed from Eq. (38) corresponds to the eigenmode $m = 0$ and $q = 0.2$ for a shape parameter $\mu_0 = 86$ nm. For comparison, the radiative decay rate (red) for plasmons excited on a prolate spheroidal surface is computed using Eq. (42) for $\zeta_0 = 65$ nm and $m = 0, l = 1$, corresponding to the dipolar mode. To facilitate visual comparison within the same plot window, note that the spheroidal case for $m = 0$ (right) has been multiplied by 0.006 and for the case $m = 1$ (left) by 0.01. The composition of the specific parameters for comparison was guided by the potential distribution in each case.

$\mathcal{I}_{m\lambda}^{(2)}$ given by Eq. (25), the p polarization. Inspecting the integrands for their convergence, we compute the integrals using an iterative numerical integration scheme (Runge-Kutta) due to lack of fast oscillations. The result is shown in Fig. 3. Note that to facilitate visual comparison within the same plot window, the radiative decay rate for prolate spheroid for modes $m = 0$ and $m = 1$ have been multiplied by 0.006 and 0.01, respectively. The effect of higher index modes λ, q , and l with the same azimuthal order m on radiative decay rate per solid angle may also be studied, as shown in Fig. 4. As one may expect from the nearfield patterns of higher λ , and q , analogous to $l = 2$, a quadrupolar pattern appears for the emitted photons. Here, it is understood that an angular segment is occupied by the probe itself, as opposed to the $0-2\pi$ range for the finite volume spheroidal systems. It is

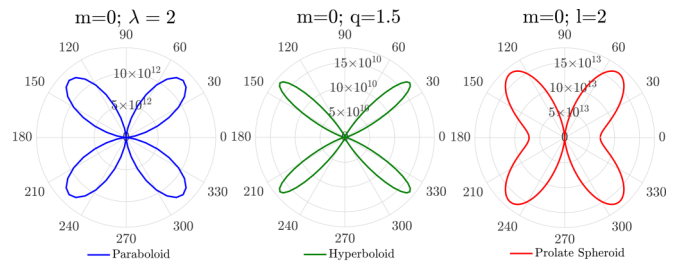


FIG. 4. Comparison of the higher-order modes' radiative decay rates for the three different cases described in Fig. 3. In the case of the prolate spheroidal plasmons, the emitted radiation pattern corresponds to the quadrupolar charge density oscillations.

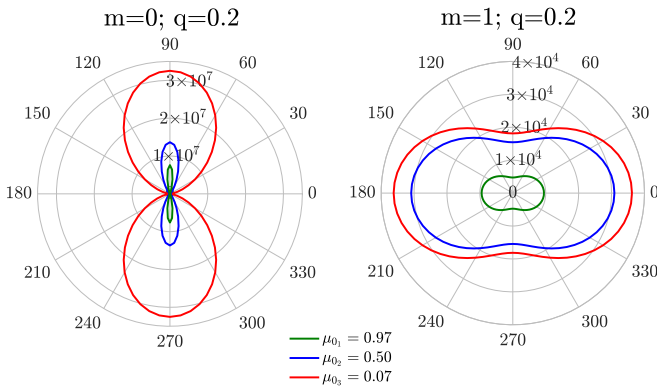


FIG. 5. Curvature induced shift in the radiation pattern associated with the decay of plasmons excited on the hyperboloidal surfaces for the modes $m = 0$ (left) and $m = 1$ (right) and $q = 0.2$. To facilitate comparison within the same plot window, the case for μ_1 has been multiplied by 20 (left) and by 50 (right).

further understood that for larger particles or probe apex size retardation effects may modify the higher-order modes.

The dependence of the radiative decay rate upon the parameter that sets the boundary, allows for control of the curvature and thus the photon emission pattern. As can be seen from Fig. 5, for the $m = 0$ mode, the higher the curvature of the hyperboloidal apex, the lower the amplitude and the narrower the angular distribution of the emitted photons. Moreover, for the $m = 1$ the higher curvature while resulting in a lower amplitude does not result in a higher angular confinement.

VI. CONCLUSIONS

The presented quantization of charge density oscillations on the surface of geometric entities with local curvature but with an extended dimension constitutes first time results with potential for modeling quantum effects in plasmonics. The obtained analytical expressions for the operators associated with surface plasmon quantities, help calculating interactions with other quantized fields, e.g., the interaction of the probe with a nearby quantum emitter, or with the radiation field of a quantum dipole. Owing to their apex symmetry and curvature, the comparison of the calculated quantities show that hyperboloidal and paraboloidal plasmons qualitatively exhibit similar dispersion relations and radiative decay rates. We conclude that, the quantitative differences observed in the allowed resonance values of the dielectric function and the emitted radiation patterns are therefore primarily attributed to the difference in curvature in the asymptotic region, away from the apex. From a comparison with the modes excited on a prolate spheroidal surface, for which experimentally typically only low energy dipolar and quadrupolar eigenmodes or their mixtures have been observed to contribute to far field radiation in the visible spectrum, we expect that also only low lying modes will contribute to the emission spectra of the probe. Unlike the all discrete spectrum of the quantum numbers associated with the spheroidal modes, the eigenvalues characterizing the hyperboloidal or paraboloidal plasmons along their infinite dimensions exhibit a continuous spectrum, making a direct comparison of plasmon wave vectors unclear.

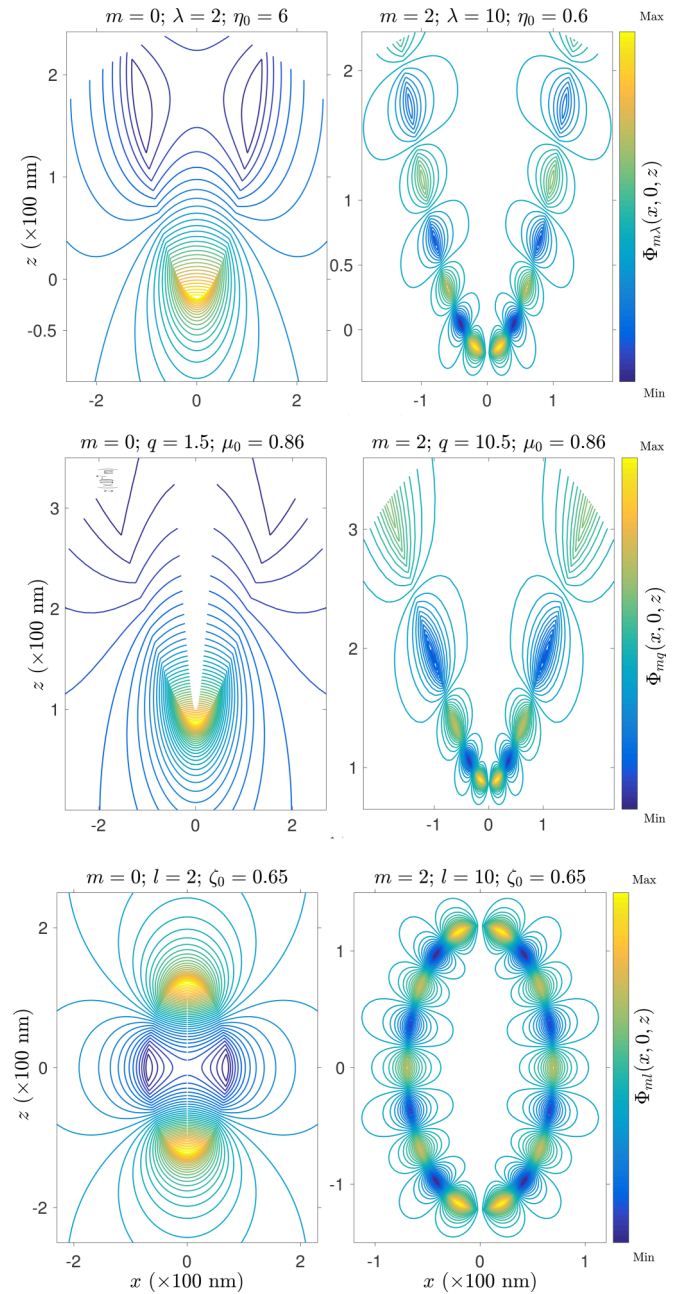


FIG. 6. The spatial distribution of low and high lying eigenmodes of the quasistatic electric potential for the three modeling domains investigated. For the same mode index m , optimizing the apex curvature overlap within the same spatial zx domains, and analyzing the potential distribution, leads to the determination of the corresponding continuous eigenvalues λ of the paraboloid (top) and q of the hyperboloid (middle), respectively, as well as the discrete eigenvalue l of the prolate spheroid (bottom). The geometric parameters η_0 , μ_0 , and ζ determines the form of the considered domains. For proper geometric and modal adjustments, the similarities in the potential distributions are clearly evident from the contour plots. The discontinuity in the contour lines near the symmetry axis of the hyperboloids is due to the singularity in the conical functions there.

However, visualization of the eigenmode field patterns, that is, how the fields fluctuate for given continuous eigenvalues in the case of hyperboloids and paraboloids, can facilitate the

comparison with the discrete eigenvalues for the spheroidal case. For a given set of eigenmodes, photon emission from the higher apex curvature tips occurs with a more localized radiation pattern. Following the presented results for the allowed values of the dielectric functions $\varepsilon_{ml}(\zeta_0)$, $\varepsilon_{m\lambda}(\eta_0)$, and $\varepsilon_{mq}(\mu_0)$, the corresponding dispersion relations and radiative decay rates can be obtained for real materials from a comparison with the experimentally determined optical properties of solids (such the compilation by Hageman [28] or by Palik [29]). In summary, the presented results can aid the design and fabrication of tips with specific photonic and plasmonic characteristics. For example, for a gold or silver tip, such as those used in electron emission experiments [23], using the presented results one may determine both the fabrication design parameters and the excitation laser wavelength and polarization. In such applications, a comparison of Figs. 2 and 7 with the optical properties of, for example silver [28], indicates the availability of several resonance modes in the visible. The results can help the analysis of the radiation emitted from the nanotips as a result of electron or photon scattering, which are of importance to plasmonics in experiments such as EELS (electron energy loss spectroscopy) and SPM. For a specific material typically employed in plasmonics such as gold and silver, the results offer estimates of the polarization, angular, and spectral properties of the emitted radiation. In such instances, the emitted photons may be analyzed for the specific eigenmode of charge density oscillation (m, λ) that created them. In light of the obtained multiparameter dependence, any agreement with the theory would require fabrication control of the geometric features of the nanostructure.

The Department of Energy will provide public access to these results of federally sponsored research in accordance with the DOE Public Access Plan [30].

ACKNOWLEDGMENTS

This work was supported in part by the laboratory directed research and development (LDRD) fund at Oak Ridge National Laboratory (ORNL). ORNL is managed by UT-Battelle, LLC, for the US DOE under Contract DE-AC05-00OR22725. This manuscript has been authored by UT-Battelle, LLC under Contract No. DE-AC05-00OR22725 with the U.S. Department of Energy. The United States Government retains and the publisher, by accepting the article for publication, acknowledges that the United States Government retains a non-exclusive, paid-up, irrevocable, worldwide license to publish or reproduce the published form of this manuscript, or allow others to do so, for United States Government purposes.

APPENDIX A

In Appendix A, we provide the detailed calculations for the formulas and results claimed in Sec. II. The paraboloidal domain allows the parametric study of the various scattering processes as functions of the local curvature without

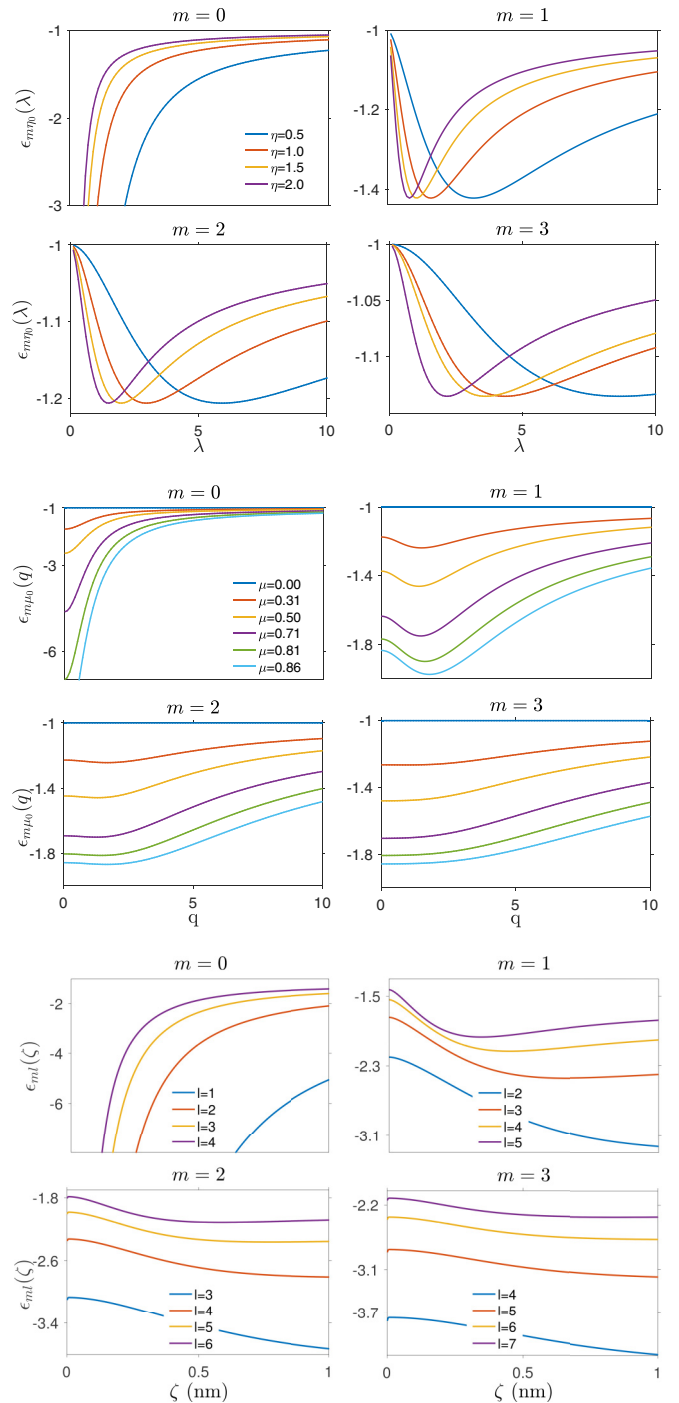


FIG. 7. Paraboloidal, hyperboloidal, and prolate spheroidal non-retarded surface plasmon dispersion relations. The resonance values of the dielectric function ε are shown for low lying modes as a function of the continuous eigenvalue λ for a paraboloid (top) and q for a hyperboloid (middle), and as a function of the shape parameter ζ for a prolate spheroid. The surfaces of the paraboloid and hyperboloids are set by the parameter η_0 and μ_0 , respectively, while ζ defines the form of the spheroidal surface (bottom). The discrete modes are denoted by m for the azimuthal oscillations and by l in the spheroidal case.

displacement of the domain. The quasistatic solution of the electric scalar potential near a paraboloidal domain has been reported in Ref. [31]. The paraboloidal coordinates (ξ, η, φ) , are related to the rectangular coordinates by

$$x = a \xi \eta \cos \varphi, \quad y = a \xi \eta \sin \varphi, \quad z = \frac{a}{2} (\xi^2 - \eta^2), \quad (\text{A1})$$

with the corresponding scale factors

$$h_\xi = h_\eta = a\sqrt{\xi^2 + \eta^2} \quad \text{and} \quad h_\varphi = a\xi\eta, \quad (\text{A2})$$

where $0 \leq \varphi < 2\pi$ denotes the usual azimuthal angle, $a > 0$ is a dimensionless constant to be determined later, and the two coordinates $\eta, \xi \geq 0$ are such that the surfaces of constant $\eta > 0$ and $\xi > 0$ describe upward and downward paraboloids of revolution about the z -axis, respectively.

Laplacian is given by

$$\begin{aligned} \vec{\nabla}^2 = & \frac{1}{a^2(\xi^2 + \eta^2)} \left[\frac{\partial^2}{\partial \xi^2} + \frac{1}{\xi} \frac{\partial}{\partial \xi} + \frac{\partial^2}{\partial \eta^2} \right. \\ & \left. + \frac{1}{\eta} \frac{\partial}{\partial \eta} + \left(\frac{1}{\xi^2} + \frac{1}{\eta^2} \right) \frac{\partial^2}{\partial \varphi^2} \right]. \end{aligned} \quad (\text{A3})$$

Assuming the ansatz [14] $\Phi(\xi, \eta, \varphi) = F(\lambda\xi)G(\lambda\eta)e^{im\varphi}$, F satisfies the Bessel equation:

$$\left[\frac{d^2}{d\xi^2} + \frac{1}{\xi} \frac{d}{d\xi} + \left(1 - \frac{m^2}{\xi^2} \right) \right] F_m(\lambda\xi) = 0, \quad (\text{A4})$$

with the Bessel functions of the first and second kind $J_m(\lambda\xi)$ and $Y_m(\lambda\xi)$ forming a set of solutions, allowing us to express any general solution in terms of these functions. Likewise, G satisfies the modified Bessel equation:

$$\left[\frac{d^2}{d\eta^2} + \frac{1}{\eta} \frac{d}{d\eta} - \left(1 + \frac{m^2}{\eta^2} \right) \right] G_m(\lambda\eta) = 0, \quad (\text{A5})$$

with now the modified Bessel Functions $I_m(\lambda\eta), K_m(\lambda\eta)$ forming the basis for our solutions.

Calculation of $\vec{\nabla}^2\Phi$. The potential Φ could be written as

$$\Phi = \Theta(\eta_0 - \eta)\Phi_i(\mathbf{r}, t) + \Theta(\eta - \eta_0)\Phi_o(\mathbf{r}, t),$$

where the inside and outside potentials Φ_i and Φ_o are given by Eq. (1). The Laplacian of Φ in paraboloidal coordinates is given by Eq. (A3). Since the Heaviside function depends on the coordinate η , we only need to consider $\partial\Phi/\partial\eta$ and $\partial^2\Phi/\partial\eta^2$ as the partial derivatives of Φ with respect to the other coordinates ξ and φ can be trivially expressed in terms the corresponding partials of Φ_i and Φ_o , respectively. Using the fact that the derivative of Heaviside function is the Dirac delta function δ (in the distributional sense), one finds

$$\begin{aligned} \frac{\partial\Phi}{\partial\eta} = & \Theta(\eta_0 - \eta) \frac{\partial\Phi_i}{\partial\eta} + \Theta(\eta - \eta_0) \frac{\partial\Phi_o}{\partial\eta} \\ & - \delta(\eta_0 - \eta)\Phi_i + \delta(\eta - \eta_0)\Phi_o, \end{aligned} \quad (\text{A6})$$

where the last two terms of the above expression vanish due to the fact that $\Phi_i = \Phi_o$ at the boundary $\eta = \eta_0$. Thus

$$\frac{\partial\Phi}{\partial\eta} = \Theta(\eta_0 - \eta) \frac{\partial\Phi_i}{\partial\eta} + \Theta(\eta - \eta_0) \frac{\partial\Phi_o}{\partial\eta} \quad (\text{A7})$$

and as a result

$$\begin{aligned} \frac{\partial^2\Phi}{\partial\eta^2} = & \Theta(\eta_0 - \eta) \frac{\partial^2\Phi_i}{\partial\eta^2} + \Theta(\eta - \eta_0) \frac{\partial^2\Phi_o}{\partial\eta^2} \\ & - \delta(\eta_0 - \eta) \frac{\partial\Phi_i}{\partial\eta} + \delta(\eta - \eta_0) \frac{\partial\Phi_o}{\partial\eta}. \end{aligned} \quad (\text{A8})$$

Substituting Eqs. (A7) and (A8), together with partials derivatives of Φ with respect to ξ and φ , into the Laplacian Eq. (A3) gives

$$\begin{aligned} \vec{\nabla}^2\Phi = & \frac{1}{a^2(\xi^2 + \eta^2)} \left[\delta(\eta - \eta_0) \left(\frac{\partial\Phi_o}{\partial\eta} - \frac{\partial\Phi_i}{\partial\eta} \right) \right. \\ & \left. + \Theta(\eta_0 - \eta) \vec{\nabla}^2\Phi_i + \Theta(\eta - \eta_0) \vec{\nabla}^2\Phi_o \right]. \end{aligned} \quad (\text{A9})$$

Treating the above expression in the sense of a distribution in η only and noting that $\vec{\nabla}^2\Phi_i$ and $\vec{\nabla}^2\Phi_o$ vanish for $\eta < \eta_0$ and $\eta > \eta_0$, respectively, we obtain the claimed identity Eq. (2) for the Laplacian of Φ .

From Eq. (2), one can solve for the charge density to obtain

$$\sigma = - \frac{1}{4\pi a\sqrt{\xi^2 + \eta^2}} \left(\frac{\partial\Phi_o}{\partial\eta} - \frac{\partial\Phi_i}{\partial\eta} \right) \Big|_{\eta=\eta_0}. \quad (\text{A10})$$

The expression on the right-hand side of Eq. (A10) can be easily calculated from Eq. (1) as

$$\begin{aligned} & \left(\frac{\partial\Phi_o}{\partial\eta} - \frac{\partial\Phi_i}{\partial\eta} \right) \Big|_{\eta=\eta_0} \\ & = \sum_{m,p} S_m^p(\varphi) \int_0^\infty \lambda A_{m\lambda p}(t) J_m(\lambda\xi) \mathcal{W}_m(\lambda\eta_0) d\lambda, \end{aligned} \quad (\text{A11})$$

where $\mathcal{W}_m(\cdot)$ denotes the Wronskian given by

$$\mathcal{W}_m(z) = I_m(z)K'_m(z) - I'_m(z)K_m(z). \quad (\text{A12})$$

In view of the identity $\mathcal{W}_m(z) = -\frac{1}{z}$ ($z \neq 0$) for the modified Bessel functions [14], and from Eqs. (A10) and (A12) we obtain Eq. (3).

Calculation of the potential energy V . The potential energy is given by

$$\begin{aligned} V = & \frac{1}{2} \int_{\eta=\eta_0} \sigma \Phi_i|_{\eta=\eta_0} dS \\ = & \frac{1}{2} \int_0^{2\pi} \int_0^\infty \sigma \Phi_i|_{\eta=\eta_0} h_\xi h_\varphi d\xi d\varphi. \end{aligned} \quad (\text{A13})$$

From Eq. (1), the potential $\Phi_i|_{\eta=\eta_0}$ is given by

$$\begin{aligned} \Phi_i|_{\eta=\eta_0} = & \sum_{m,p} S_m^p(\varphi) \int_0^\infty A_{m\lambda p}(t) I_m(\lambda\eta_0) \\ & \times K_m(\lambda\eta_0) J_m(\lambda\xi) d\lambda. \end{aligned} \quad (\text{A14})$$

Substituting Eq. (A14) and the expressions for $\sigma, h_\xi,$ and h_φ from Eqs. (5) and (A2) into the above integral for V

gives

$$V = \frac{a}{8\pi} \sum_{m', p'} \sum_{m, p} \int_0^\infty \int_0^{2\pi} S_m^p(\varphi) S_{m'}^{p'}(\varphi) \times \left[\int_0^\infty A_{m'\lambda'p'}(t) I_{m'}(\lambda'\eta_0) K_{m'}(\lambda'\eta_0) J_{m'}(\lambda'\xi) d\lambda' \times \int_0^\infty A_{m\lambda p}(t) J_m(\lambda\xi) d\lambda \right] \xi d\varphi d\xi. \quad (\text{A15})$$

Using the orthogonality relation for $\{S_m^p\}_{m, p}$,

$$\int_0^{2\pi} S_m^p(\varphi) S_{m'}^{p'}(\varphi) d\varphi = \pi \delta_{mp} \delta_{mm'} \delta_{pp'}, \quad (\text{A16})$$

where

$$\delta_{mp} = 4\delta_{0p} + \delta_{1p} - 2\delta_{m0}\delta_{0p}, \quad (\text{A17})$$

we can write Eq. (A15) as

$$V = \frac{a}{8} \sum_{m, p} \hat{\delta}_{mp} \int_0^\infty \left[\int_0^\infty A_{m'\lambda'p'}(t) I_{m'}(\lambda'\eta_0) K_{m'}(\lambda'\eta_0) \times J_m(\lambda'\xi) d\lambda' \int_0^\infty A_{m\lambda p}(t) J_m(\lambda\xi) d\lambda \right] \xi d\xi. \quad (\text{A18})$$

Finally, in view of the orthogonality relation for Bessel functions given by Eq. (11.59) [16]

$$\int_0^\infty \xi J_m(\lambda\xi) J_m(\lambda'\xi) d\xi = \frac{\delta(\lambda - \lambda')}{\lambda}, \quad (\text{A19})$$

for $m \geq -1$, and $\lambda, \lambda' > 0$, we obtain Eq. (8).

Note that in the above calculations, we have changed the order of integration to simplify the obtained expressions. This is done in view of the Fubini's theorem based on the absolute integrability of the above expressions. Our argument is based on the asymptotic behavior of Bessel functions, see [14], Eqs. (5.11.6), (5.11.8), and (5.11.9), and the fact that the potential, and thus Eq. (1), is finite in the entire space. The mathematical details, however, is beyond the scope of this paper, and is therefore omitted. The same argument is also used in the other cases using the asymptotic behavior of the corresponding eigenfunctions, but has been omitted in this presentation.

Calculation of the kinetic energy T . Comparing the expression for Ψ given by Eq. (9) with the inside potential given by Eq. (1), it is clear that Ψ also satisfies the Laplace equation $\bar{\nabla}^2 \Psi = 0$. Using the vector identity $\bar{\nabla} \Psi \cdot \bar{\nabla} \Psi = \bar{\nabla} \cdot (\Psi \bar{\nabla} \Psi) - (\Psi \bar{\nabla}^2 \Psi)$, together with the fact $\bar{\nabla}^2 \Psi = \frac{d}{dt} \bar{\nabla}^2 \Psi = 0$, it follows that $\bar{\nabla} \Psi \cdot \bar{\nabla} \Psi = \bar{\nabla} \cdot (\Psi \bar{\nabla} \Psi)$, and, as a consequence,

$$\dot{\mathbf{u}} \cdot \dot{\mathbf{u}} = \frac{e^2}{m_e^2} \bar{\nabla} \cdot (\Psi \bar{\nabla} \Psi). \quad (\text{A20})$$

Next, we substitute Eq. (A20) in the expression for T and apply Gauss's theorem to obtain

$$T = \frac{e^2 n_0}{2m_e} \int_{\text{surf.}} (\Psi \bar{\nabla} \Psi) \Big|_{\eta=\eta_0} \cdot \hat{\mathbf{n}} dA, \quad (\text{A21})$$

where, as in the case of potential V , the integral is taken over the surface $\eta = \eta_0$ with the surface area element

$dA = h_\xi h_\varphi d\xi d\varphi$. Using the formula for gradient in the paraboloidal coordinates and noting $\hat{\mathbf{n}} = \mathbf{e}_\eta$ on the surface, one gets

$$T = \frac{e^2 n_0}{2m_e} \int_0^{2\pi} \int_0^\infty \left(\Psi \frac{1}{h_\eta} \frac{\partial \Psi}{\partial \eta} \right) \Big|_{\eta=\eta_0} h_\xi h_\varphi d\xi d\varphi. \quad (\text{A22})$$

Using the definition of Ψ given by Eq. (9) and the expressions for the scale factors Eq. (A2), the right-hand side of Eq. (A22) can be written as

$$T = a\eta_0 \frac{e^2 n_0}{2m_e} \sum_{m, p} \sum_{m', p'} \int_0^{2\pi} S_m^p(\varphi) S_{m'}^{p'}(\varphi) d\varphi \times \int_0^\infty \left[\int_0^\infty \frac{\dot{B}_{mp\lambda}(t)}{\omega_{m\lambda}^2} J_m(\lambda\xi) I_m(\lambda\eta_0) K_m(\lambda\eta_0) d\lambda \times \int_0^\infty \lambda \frac{\dot{B}_{m'p'\lambda'}(t)}{\omega_{m'\lambda'}^2} J_{m'}(\lambda'\xi) I_{m'}(\lambda'\eta_0) K_{m'}(\lambda'\eta_0) d\lambda' \right] \xi d\xi. \quad (\text{A23})$$

Invoking the orthogonality relations Eq. (A16) and Eq. (A19) in Eq. (A23) by using a similar argument as the one given for the case of the potential, it follows that

$$T = \frac{a\eta_0 \omega_p^2}{8} \sum_{m, p} \hat{\delta}_{mp} \int_0^\infty \frac{1}{\omega_{m\lambda}^4} [\dot{B}_{mp\lambda}(t)]^2 \times I_m(\lambda\eta_0) I_m'(\lambda\eta_0) [K_m(\lambda\eta_0)]^2 d\lambda. \quad (\text{A24})$$

Now in view of Eq. (6), we have

$$\eta_0 \omega_p^2 / \omega_{m\lambda}^2 = (\lambda K_m(\lambda\eta_0) I_m'(\lambda\eta_0))^{-1}.$$

This substitution in Eq. (A24) gives Eq. (10).

Interaction Hamiltonian. Briefly, the hydrodynamical formulation of the electron gas by Crowell and Ritchie [10] yields

$$\bar{\nabla} \frac{\partial}{\partial t} \Psi(\mathbf{r}, t) = -\frac{e}{m} \bar{\nabla} \Phi(\mathbf{r}, t) + \frac{\beta^2}{n_0} \bar{\nabla} n(\mathbf{r}, t), \quad \bar{\nabla}^2 \Phi(\mathbf{r}, t) = 4\pi e n(\mathbf{r}, t), \quad (\text{A25})$$

$$\bar{\nabla}^2 \Psi(\mathbf{r}, t) = \frac{\partial}{\partial t} n(\mathbf{r}, t) / n_0,$$

where $\Phi(\mathbf{r}, t)$, $\Psi(\mathbf{r}, t)$, and $n(\mathbf{r}, t)$ are the electric potential, velocity potential, and electronic density, respectively, in the electron gas, while n_0 is the electronic density in the undisturbed state of the electron gas and β is the propagation speed of the disturbance through electron gas. By linearizing these equations, employing perturbation theory, Ritchie obtained the first order interaction Hamiltonian $\mathcal{H}_i = \frac{1}{c} \int \mathbf{J} \cdot \mathbf{A} d\Omega$, where \mathbf{J} is the induced current density and \mathbf{A} is the vector potential operator of the photon field.

APPENDIX B

Appendix B provides the details for the formulas and results claimed in Sec. III. An arbitrary point in the Cartesian space can be expressed in terms of the prolate spheroidal

coordinates (η, μ, φ) [14,32] by

$$\begin{aligned} x &= z_0 \sqrt{(\eta^2 - 1)(1 - \mu^2)} \cos \varphi, \\ y &= z_0 \sqrt{(\eta^2 - 1)(1 - \mu^2)} \sin \varphi, \\ z &= z_0 \eta \mu, \end{aligned} \quad (\text{B1})$$

with the corresponding scale factors

$$\begin{aligned} h_\eta &= z_0 \sqrt{\frac{\eta^2 - \mu^2}{\eta^2 - 1}}, \\ h_\mu &= z_0 \sqrt{\frac{\eta^2 - \mu^2}{1 - \mu^2}}, \\ h_\varphi &= z_0 \sqrt{(1 - \mu^2)(\eta^2 - 1)}, \end{aligned} \quad (\text{B2})$$

where $z_0 > 0$ is an overall scale factor, $1 \leq \eta < \infty$, $-1 \leq \mu \leq 1$, and $0 \leq \varphi < 2\pi$ denotes the usual azimuthal angle. The surfaces of constant μ define hyperboloids of revolution about the z axis, while the surfaces of constant η correspond to prolate spheroids. It is often customary to use the substitutions $\sinh \zeta = \eta$ and $\sin \theta = \mu$ with $1 \leq \eta < \infty$, and $-1 \leq \mu \leq 1$; however, in this presentation the surfaces of constant coordinates are no longer geometrically meaningful.

Considering a solid hyperboloid of revolution $\mu \geq \mu_0$ ($\mu_0 > 0$) with dielectric constant ε_1 immersed in a medium whose dielectric constant ε_2 can be assumed with no loss of generality to be 1, it follows that the potential of the electric $\Phi(\mu, \eta, \varphi)$ has to satisfy the Laplace equation $\vec{\nabla}^2 \Phi = 0$ everywhere except on the boundary surface $\mu = \mu_0$, where the Laplacian is given by [14]

$$\begin{aligned} \vec{\nabla}^2 &= \frac{1}{z_0^2(\eta^2 - \mu^2)} \left\{ \frac{\partial}{\partial \eta} \left[(\eta^2 - 1) \frac{\partial}{\partial \eta} \right] + \frac{\partial}{\partial \mu} \left[(1 - \mu^2) \frac{\partial}{\partial \mu} \right] \right. \\ &\quad \left. + \left[\frac{\eta^2 - \mu^2}{(\eta^2 - 1)(1 - \mu^2)} \right] \frac{\partial^2}{\partial \varphi^2} \right\}. \end{aligned} \quad (\text{B3})$$

Assuming the ansatz [14] $\Phi(\mu, \eta, \varphi) = F(\eta)G(\mu)e^{im\varphi}$, one finds that F and G satisfy the differential equations:

$$\frac{d}{d\eta} \left[(\eta^2 - 1) \frac{dF_m}{d\eta} \right] - \frac{m^2}{\eta^2 - 1} F_m = c F_m, \quad (\text{B4})$$

$$\frac{d}{d\mu} \left[(1 - \mu^2) \frac{dG_m}{d\mu} \right] - \frac{m^2}{1 - \mu^2} G_m = -c G_m. \quad (\text{B5})$$

Letting $c = \nu(\nu + 1)$ (see Refs. [12,14,33]), where $\nu = -1/2 + iq$ and $q \in [0, \infty)$, one can obtain a continuous spectrum of real eigenvalues and eigenfunctions in terms of the associated Legendre functions or conical functions $P_{-\frac{1}{2}+iq}^m(z)$ [denoted by $P_{mq}(z)$] of complex lower index with $-\infty < z < \infty$ satisfying the orthogonality relation [12]

$$\int_1^\infty P_{mq}(\eta) P_{mq'}(\eta) d\eta = \frac{Z_q^m}{q \tanh(\pi q)} \delta(q - q'), \quad (\text{B6})$$

A bounded satisfactory real-valued solution to the first equation in Eq. (B4) is given by $P_{-\frac{1}{2}+iq}^m(\eta)$ (see [12,14,33]), whereas a pair of satisfactory real-valued solutions to the second equation in Eq. (B4) are given by $P_{-\frac{1}{2}+iq}^m(\mu)$ and

$P_{-\frac{1}{2}+iq}^m(-\mu)$ [14,26,34]. Avoiding the singularity at $\mu = -1$ [14], we shall choose the solution $P_{-\frac{1}{2}+iq}^m(\mu)$ for the inside region $\mu_0 \leq \mu \leq 1$ and $P_{-\frac{1}{2}+iq}^m(-\mu)$ for the outside region $-1 \leq \mu \leq \mu_0$. Thus the inside and outside potentials Φ_i and Φ_o are expressed as sums over the Fourier harmonics

$$\int_0^\infty A_{mq}(t) P_{-\frac{1}{2}+iq}^m(\eta) P_{-\frac{1}{2}+iq}^m(\mu) dq e^{im\varphi} \quad (\text{B7})$$

and

$$\int_0^\infty B_{mq}(t) P_{-\frac{1}{2}+iq}^m(\eta) P_{-\frac{1}{2}+iq}^m(-\mu) dq e^{im\varphi}, \quad (\text{B8})$$

respectively, where $A_{mq}(t)$ and $B_{mq}(t)$ are complex valued amplitudes and $m \in \mathbb{Z}$. Using the fact [35] that $\Gamma(1/2 + m - iq) P_{-\frac{1}{2}+iq}^m(z) = \Gamma(1/2 - m - iq) P_{-\frac{1}{2}+iq}^{-m}(z)$ for all $z \in \mathbb{R}$ and $m \geq 0$, it follows that one only needs to expand Φ_i and Φ_o in terms of $\cos m\varphi$, for $m = 0, 1, 2, \dots$. More precisely, we use the system $H_m(\varphi) = (2 - \delta_{0m}) \cos \varphi$ satisfying the orthogonality relation

$$\int_0^{2\pi} H_m(\varphi) H_{m'}(\varphi) d\varphi = \pi \hat{\delta}_{0m} \delta_{mm'}, \quad (\text{B9})$$

where

$$\hat{\delta}_{0m} = 1 + \delta_{0m}. \quad (\text{B10})$$

Finally, imposing the continuity of the potential across the boundary $\mu = \mu_0$, we find the inside and outside potentials, which are expressed in Eq. (29).

Applying the Laplacian in Eq. (B3) to the potential Eq. (29) and using a similar argument given in Eqs. (A6)–(A9), we find

$$\vec{\nabla}^2 \Phi = -\frac{1 - \mu^2}{z_0^2(\eta^2 - \mu^2)} \left(\frac{\partial \Phi_o}{\partial \mu} - \frac{\partial \Phi_i}{\partial \mu} \right) \delta(\mu - \mu_0). \quad (\text{B11})$$

Using the expressions for Φ_i and Φ_o in Eq. (29), we get

$$\begin{aligned} &\left(\frac{\partial \Phi_o}{\partial \mu} - \frac{\partial \Phi_i}{\partial \mu} \right) \Big|_{\mu=\mu_0} \\ &= \sum_m H_m(\varphi) \int_0^\infty A_{mq}(t) \times P_{mq}(\eta) \mathcal{W}_{mq}(\mu_0) dq, \end{aligned} \quad (\text{B12})$$

where $\mathcal{W}_{mq}(\mu)$ denotes the Wronskian for the conical functions

$$\mathcal{W}_{mq}(\mu) = P_{mq}(\mu) \frac{dP_{mq}(-\mu)}{d\mu} - P_{mq}(-\mu) \frac{dP_{mq}(\mu)}{d\mu}. \quad (\text{B13})$$

The exact value of Eq. (B13) is given by [12]

$$\mathcal{W}_{mq}(\mu) = \frac{2Z_q^m \cosh(\pi q)}{\pi \sqrt{1 - \mu^2}}, \quad (\text{B14})$$

where

$$Z_q^m = (-1)^m \prod_{k=1}^m \left(q^2 + \frac{(2k-1)^2}{4} \right). \quad (\text{B15})$$

APPENDIX C

Here are some relations we have used in Sec. IV. The known real spherical harmonics are given by [35]

$$Y_{lm}^p(\mu, \varphi) = \sqrt{\frac{(2 - \delta_{0m})(2l + 1)(l - m)!}{4\pi(l + m)!}} P_l^m(\mu) [\delta_p^1 \cos(m\varphi) + \delta_p^{-1} \cos(m\varphi)], \quad (C1)$$

with associated Legendre functions $P_l^m(\cdot)$ and orthogonality relation:

$$\int_0^{2\pi} \int_{-1}^1 Y_{lm}^p(\mu, \varphi) Y_{l'm'}^{p'}(\mu, \varphi) d\mu d\varphi = \delta_{ll'} \delta_{mm'} \delta_{pp'}. \quad (C2)$$

Emission matrix element in prolate spheroidal case following the same relations as in the paraboloidal and hyperboloidal cases could be obtained as

$$\mathcal{M}_{em}^{(js)} = \frac{n_0 e^2}{m_0} \sqrt{\frac{\hbar}{\nu \omega_s}} \frac{\alpha_{lmp}}{2i \omega_{lm}^2} P_l^m(\zeta_0) Q_l^m(\zeta_0) \iint (\hat{\mathbf{e}}_\eta \cdot \hat{\mathbf{e}}_j) Y_{lm}^p(\mu, \varphi) e^{-is \cdot \mathbf{r}} h_\mu h_\varphi d\mu d\varphi \Big|_{\zeta=\zeta_0}. \quad (C3)$$

The following integral identity has been used in calculation of prolate spheroidal matrix element given by Eq. (16.127) [36]:

$$e^{i\mathbf{k} \cdot \mathbf{x}} = 4\pi \sum_{l=0}^{\infty} i^l j_l(\mathbf{k}r) \sum_{m=-l}^l Y_{lm}^*(\theta, \varphi) Y_{lm}(\theta', \varphi'), \quad (C4)$$

where $j_l(\mathbf{k}r)$ is the spherical Bessel function of order l whose relation with regular Bessel function $J_l(\cdot)$ is given by

$$j_l(x) = \sqrt{\frac{\pi}{2x}} J_{l+\frac{1}{2}}(x). \quad (C5)$$

Lastly, the relations between spherical wave vectors \mathbf{s}' and \mathbf{s}'' in spherical coordinate are determined by taking the following transformations:

$$\mathbf{s}' = \frac{s_x}{\zeta_0} \vec{i} + \frac{s_y}{\zeta_0} \vec{j} + \frac{\zeta_0 s_z}{\zeta_0^2 - 1} \vec{k}, \quad (C6)$$

$$\mathbf{s}'' = \sqrt{\zeta_0^2 - 1} s_x \vec{i} + \sqrt{\zeta_0^2 - 1} s_y \vec{j} + \zeta_0 s_z \vec{k}. \quad (C7)$$

-
- [1] K. V. Garapati, M. Salhi, S. Kouckekian, G. Siopsis, and A. Passian, Poloidal and toroidal plasmons and fields of multilayer nanorings, *Phys. Rev. B* **95**, 165422 (2017).
- [2] K. V. Garapati, M. Bagherian, A. Passian, and S. Kouckekian, Plasmon dispersion in a multilayer solid torus in terms of three-term vector recurrence relations and matrix continued fractions, *J. Phys. Commun.* **2**, 015031 (2018).
- [3] E. Dumitrescu and B. Lawrie, Antibunching dynamics of plasmonically mediated entanglement generation, *Phys. Rev. A* **96**, 053826 (2017).
- [4] A. Passian and G. Siopsis, Quantum state atomic force microscopy, *Phys. Rev. A* **95**, 043812 (2017).
- [5] M. Gulde, S. Schweda, G. Storeck, M. Maiti, H. K. Yu, A. M. Wodtke, S. Schäfer, and C. Ropers, Ultrafast low-energy electron diffraction in transmission resolves polymer/graphene superstructure dynamics, *Science* **345**, 200 (2014).
- [6] M. Müller, A. Paarmann, and R. Ernstorfer, Femtosecond electrons probing currents and atomic structure in nanomaterials, *Nat. Commun.* **5**, 5292 (2014).
- [7] M. Müller, V. Kravtsov, A. Paarmann, M. B. Raschke, and R. Ernstorfer, Nanofocused plasmon-driven sub-10 fs electron point source, *ACS Photon.* **3**, 611 (2016).
- [8] A. Passian, R. H. Ritchie, A. L. Lereu, T. Thundat, and T. L. Ferrell, Curvature effects in surface plasmon dispersion and coupling, *Phys. Rev. B* **71**, 115425 (2005).
- [9] R. H. Ritchie and R. E. Wilems, Photon-Plasmon Interaction in a Nonuniform Electron Gas. I, *Phys. Rev.* **178**, 372 (1969).
- [10] J. Crowell and R. H. Ritchie, Radiative decay of Coulomb-stimulated plasmons in spheres, *Phys. Rev.* **172**, 436 (1968).
- [11] S. N. Krivoschapko and V. N. Ivanov, *Encyclopedia of Analytical Surfaces* (Springer, Cham, Switzerland, 2015).
- [12] A. Passian, S. Kouckekian, S. Yakubovich, and T. Thundat, Properties of index transforms in modeling of nanostructures and plasmonic systems, *J. Math. Phys.* **51**, 023518 (2010).
- [13] P. M. C. Morse and H. Feshbach, *Methods of Theoretical Physics*, International Series in Pure and Applied Physics Vol. 2 (McGraw-Hill, New York, 1953).
- [14] N. N. Lebedev, in *Special Functions & Their Applications*, translated and edited by R. A. Silverman, Dover Books on Mathematics (Dover Publications, New York, 1972).
- [15] F. Bowman, *Introduction to Bessel Functions*, Dover Books on Mathematics (Dover Publications, New York, 2012).
- [16] G. B. Arfken and H. J. Weber, *Mathematical Methods for Physicists* (Elsevier Science, Amsterdam, 2013).
- [17] R. H. Ritchie, J. C. Ashley, and T. L. Ferrell, The interaction of photons with surface plasmons, in *Electromagnetic Surface Modes*, edited by A. D. Boardman (Wiley, Chichester, 1982), Chap. 2.
- [18] S. S. Schweber, *An Introduction to Relativistic Quantum Field Theory* (Dover Publications, New York, 2011).

- [19] J. W. Little, T. L. Ferrell, T. A. Callcott, and E. T. Arakawa, Radiative decay of surface plasmons on oblate spheroids, *Phys. Rev. B* **26**, 5953 (1982).
- [20] R. Bennett, T. A. Barlow, and A. Beige, A physically motivated quantization of the electromagnetic field, *Eur. J. Phys.* **37**, 014001 (2016).
- [21] A. V. Belinsky, On the possibility of an incorrect choice of a quantization volume, *Moscow Univ. Phys. Bull.* **72**, 76 (2017).
- [22] E. Zeidler, *Quantum Field Theory II: Quantum Electrodynamics* (Springer, Berlin, Heidelberg, 2009).
- [23] S. Keramati, A. Passian, V. Khullar, P. Lougovski, and H. Batelaan, Low power laser-driven electron source based on plasmon enhanced metalized optical fiber tips, in 49th Annual Meeting of the APS Division of Atomic, Molecular and Optical Physics APS Meeting, Bulletin of the American Physical Society, 2018 (AIP, 2018).
- [24] A. Gil, J. Segura, and N. M. Temme, An improved algorithm and a Fortran 90 module for computing the conical function $P - 1/2 + i\tau m(x)$, *Comput. Phys. Commun.* **183**, 794 (2012).
- [25] K. S. Kölblig, A program for computing the conical functions of the first kind $P_m - 1/2 + i\tau(x)$ for $m = 0$ and $m = 1$, *Comput. Phys. Commun.* **23**, 51 (1981).
- [26] M. I. Zhurina and L. N. Karmazina, *Tables of The Legendre Functions $P_{1/2+it}(x)$: Mathematical Tables Series Part I* (Elsevier Science, Amsterdam, 2016).
- [27] M. Abramowitz and I. A. Stegun, *Handbook of Mathematical Functions: with Formulas, Graphs, and Mathematical Tables*, Dover Books on Mathematics (National Bureau of Standards, Washington, 1970).
- [28] H. J. Hagemann, W. Gudat, and C. Kunz, Optical constants from the far infrared to the x-ray region: Mg, Al, Cu, Ag, Au, Bi, C, and Al₂O₃, *J. Opt. Soc. Am.* **65**, 742 (1975).
- [29] E. D. Palik, *Handbook of Optical Constants of Solids, Five-Volume Set: Handbook of Thermo-Optic Coefficients of Optical Materials with Applications* (Elsevier Science, Amsterdam, 1997).
- [30] <http://energy.gov/downloads/doe-public-access-plan>.
- [31] A. B. Petrin, Extremely tight focusing of light at the nanoapex of a metal microtip, *Quantum Electron.* **46**, 159 (2016).
- [32] N. N. Lebedev, I. P. Skalskaya, and I. A. S. Uflyand, in *Worked Problems in Applied Mathematics*, translated by R. A. Silverman, Dover Books on Mathematics (Dover Publications, New York, 1979).
- [33] N. A. Belova, and I. A. S. Uflyand, Dirichlet problem for a toroidal segment, *J. Appl. Math. Mech.* **31**, 59 (1967).
- [34] M. I. Zhurina and L. N. Karmazina, in *Tables of the Legendre Functions $P_{-1/2+i[\tau]}(\cdot)$ Part II*, translated by D. E. Brown (The Macmillan Company, New York, 1965).
- [35] I. S. Gradshteyn and I. M. Ryzhik, *Table of Integrals, Series, and Products* (Academic Press, New York, 2014).
- [36] J. D. Jackson, *Classical Electrodynamics* (Wiley, New York, 1975).